© 2019. Published by The Company of Biologists Ltd | Development (2019) 146, dev164145. doi:10.1242/dev.164145

RESEARCH ARTICLE

Destruction complex dynamics: Wnt/β-catenin signaling alters Axin-GSK3β interactions *in vivo*

Daniel B. Lybrand[1,2,*], Misha Naiman[1,2,*], Jessie May Laumann[1], Mitzi Boardman[1], Samuel Petshow[1], Kevin Hansen[1], Gregory Scott[1] and Marcel Wehrli[1,3,‡]

ABSTRACT

The central regulator of the Wnt/β-catenin pathway is the Axin/APC/GSK3β destruction complex (DC), which, under unstimulated conditions, targets cytoplasmic β-catenin for degradation. How Wnt activation inhibits the DC to permit β-catenin-dependent signaling remains controversial, in part because the DC and its regulation have never been observed *in vivo*. Using bimolecular fluorescence complementation (BiFC) methods, we have now analyzed the activity of the DC under near-physiological conditions in *Drosophila*. By focusing on well-established patterns of Wnt/Wg signaling in the developing *Drosophila* wing, we have defined the sequence of events by which activated Wnt receptors induce a conformational change within the DC, resulting in modified Axin-GSK3β interactions that prevent β-catenin degradation. Surprisingly, the nucleus is surrounded by active DCs, which principally control the degradation of β-catenin and thereby nuclear access. These DCs are inactivated and removed upon Wnt signal transduction. These results suggest a novel mechanistic model for dynamic Wnt signal transduction *in vivo*.

KEY WORDS: Axin, *Drosophila*, GSK3, Wnt signaling, β-Catenin, Destruction complex

INTRODUCTION

Wnt-directed signal transduction is a highly conserved mechanism that controls cellular patterning, tissue development, stem cell maintenance and tissue repair in all animals (Clevers and Nusse, 2012). In the canonical Wnt pathway, β-catenin (Armadillo in *Drosophila*) functions as the primary effector: in the absence of Wnt ligand, β-catenin signaling is blocked via the 'destruction complex' (DC), which constitutively directs the degradation of newly synthesized β-catenin. This multi-protein complex contains the scaffold protein Axin, the tumor suppressor Adenomatous Polyposis Coli (APC) and Glycogen Synthase Kinase 3β (GSK3β; Shaggy, Sgg, in *Drosophila*). In contrast, when Wnt ligands are present (Wingless, Wg, in *Drosophila*), they bind and activate heteromeric receptor complexes comprising Frizzled and LRP5/6 proteins (Arrow in *Drosophila*), initiating a signaling response via the cytoplasmic transducer Dishevelled (Dsh) that ultimately inhibits the DC. As a result, β-catenin accumulates, translocates to the nucleus, and activates target gene transcription. Regulation of Wnt signaling must be precisely controlled and modulated, as deregulation leads to developmental defects or initiation of diseases including osteoporosis and many forms of cancer (Clevers and Nusse, 2012).

Although this model of Wnt signaling is now generally accepted, key aspects of how the DC is regulated remain controversial. At least a dozen models have been postulated to explain β-catenin regulation (Baig-Lewis et al., 2007; Cliffe et al., 2003; Itoh et al., 2005; Lee et al., 2003; Liu et al., 1999; Mao et al., 2002; Park et al., 2006; Rosin-Arbesfeld et al., 2000; Swarup and Verheyen, 2012; Tamai et al., 2004; Tolwinski and Wieschaus, 2001; Valvezan et al., 2012; Huang et al., 2009), including DC inactivation by kinase inhibition, complex dissociation, separation of the DC from the ubiquitylation machinery and aggregation of the complex at the site of activated receptors (Bilic et al., 2007; Li et al., 2012; Piao et al., 2008; Roberts et al., 2011; Schwarz-Romond et al., 2007b; Schwarz-Romond et al., 2007a). Much of this uncertainty derives from the fact that most components of the DC are multifunctional (serving roles apart from Wnt signaling), such that only a small fraction of the total cytoplasmic pool of each protein actually participates in Wnt signaling (Papadopoulou et al., 2004). Consequently, many investigations of the DC have resorted to protein overexpression assays in highly artificial *in vitro* systems, rendering their physiological significance uncertain. Arguably, the single most important advance toward understanding the core mechanisms of the Wnt pathway would be to observe signal transduction *in vivo*. To date, the DC has only been demonstrated biochemically, as conventional imaging strategies have been unable to differentiate functional components of the complex from larger cytoplasmic pools of these proteins. To address this issue, we have adapted bimolecular fluorescence complementation (BiFC) technology to visualize DCs under physiological conditions *in vivo*, permitting an analysis of their dynamic responses to Wnt signaling. We describe two BiFC complexes, which report both the active DC and the inactivated DC. We show that active DCs surround the nucleus. Wnt ligand triggers recruitment of these DCs to activated receptors where a conformational change causes DC inactivation. In turn, DCs dissociate from the receptor and assemble into super-complexes that accumulate α- and β-catenin. Using a pulse of Wnt to induce a signaling burst, we are able to detect short-lived DC intermediates that differ from the long-lived abundant complexes that predominate at a steady state and may be subject to modulation and feedback regulation. Thus, the ability to detect signaling complexes *in vivo* and under normal developmental conditions allows us to compare the earliest events following receptor activation to steady-state signaling. Moreover, this approach can be used to distinguish the core Wnt signaling mechanism required for the canonical pathway from accessory mechanisms that may modulate this core pathway in specific cellular contexts.

[1]Dept. of Integrative Biosciences, School of Dentistry, Oregon Health and Science University, Portland, OR 97239, USA. [2]Reed College, Portland, OR 97202, USA. [3]Knight Cancer Institute, Portland, OR 97239, USA.
*These authors contributed equally to this work

‡Author for correspondence (wehrlim@ohsu.edu)

D.B.L., 0000-0003-3010-2203; M.N., 0000-0002-4052-8534; J.M.L., 0000-0002-7936-0783; M.B., 0000-0001-9713-2103; S.P., 0000-0002-7989-3598; G.S., 0000-0003-0830-5557; M.W., 0000-0002-6805-0421

Received 5 February 2018; Accepted 5 June 2019

Development (2019) 146, dev164145. doi:10.1242/dev.164145

RESULTS

Drosophila expressing BiFC constructs develop normally

The *Drosophila* wing develops from a pseudostratified columnar epithelium: the wing imaginal disc. Unusual for this type of epithelium, nuclei are packed into the apical half; we refer to this region as the nuclear layer. Wg-expressing cells form a band about four cells wide that bisects the wing pouch and establishes a long-range Wg gradient (Fig. 1A-E, Fig. S2A). This Wg gradient activates the signaling pathway within receiving cells, which inactivates the DC, thereby creating a complementary gradient of active DC (Fig. 1C2,C3). The Wg signaling gradient induces target gene expression within the developing wing disc. For example, Distal-less (Dll) follows the Wg gradient (Fig. 1A-D). For clarity, the position of orientation of images shown in Figs 1–6 is schematically indicated in Figs S6 and S7.

Previous studies outline the functional requirements for Wg in this process, establishing the wing disc as an ideal *in vivo* model for analyzing mechanisms of long-range Wnt patterning (e.g. Neumann and Cohen, 1997; Struhl and Basler, 1993). However, these studies focus on downstream effects of manipulating Wg signaling (e.g.

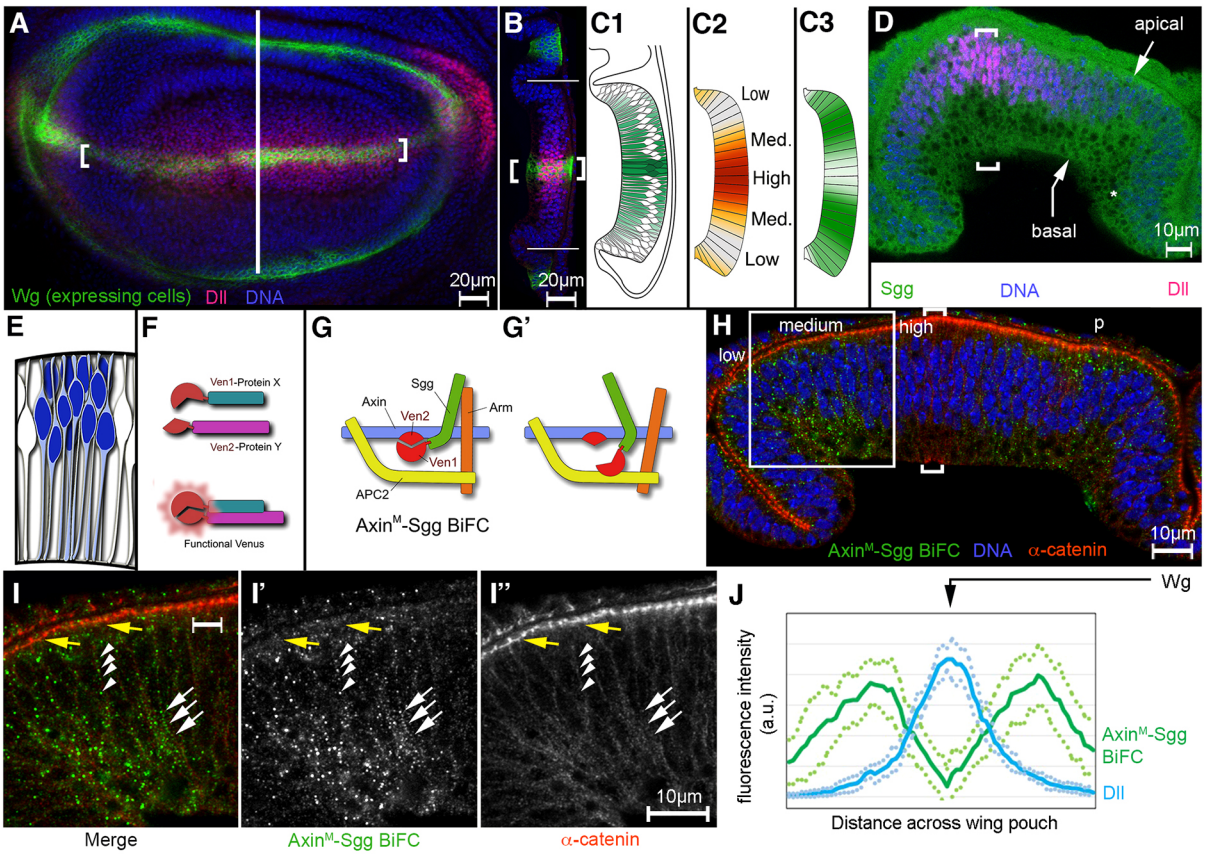

Fig. 1. Visualization of active DC *in vivo*. (A) Top-down view of *Drosophila* wing imaginal disc stained for Wg (green, brackets, see Fig. S2A for schematic), Dll (magenta) and DNA (blue). A vertical line indicates the position of the cryosection in B. (B) Transverse cryosection of wing imaginal disc (staining as in A). The wing pouch boundary is indicated (white horizontal lines). (C) Schematic of the Wg-dependent gradients across the wing pouch. (C1) Schematic of the pseudostratified epithelium. Wg-producing cells (green) flank the dorsoventral boundary and secrete Wg, establishing a gradient across the wing pouch. (C2) The Wg gradient is translated into an intracellular gradient of signaling activity (red to white, indicating high, medium and low pathway activation), which generates a predicted inverse distribution of active DC (green) (C3). (D) Transverse cryosection of wing imaginal disc stained for Sgg (green), Dll (magenta) and DNA (blue). Wg-expressing cells are in brackets; see Fig. S2D for gray scale. Unstained areas (asterisk) are vacuolar varicosities of unknown origin, possibly arising during sample preparation (n=6). (E) Schematic representation of wing disc cells. Nuclei are the largest structure (~4.5 μm tall, ~2 μm wide; blue), surrounded by a thin layer of cytoplasm. These cell bodies are tightly packed in the apical half of the epithelium. Cells extend to apical and basal surfaces of the epithelium, accounting for an epithelial height of ~28-35 μm. (F) Schematic of the BiFC protocol, whereby two fragments of Venus (Ven) fluorescent protein expressed as fusion constructs with two proteins of interest (X and Y) fold into a functional Venus protein upon interaction of fusion partners. (G,G′) Schematic of the Axin^{M}-Sgg BiFC interaction in the DC, where internally tagged Axin interacts with C-terminally tagged Sgg to yield BiFC fluorescence (G) but only if DC conformation allows for it (G versus G′). (H,I) Ubiquitous expression of Axin^{M}-Ven2 and Sgg-Ven1 (via the tubulin-α1 promotor) produces graded Axin^{M}-Sgg BiFC signals (green), indicating the distribution of active DC. BiFC signals are low near Wg-expressing cells (brackets) and increase with distance. Cell outlines are indicated by α-catenin (red); nuclei are in blue. The box in H marks the position of the inset magnified in I. Axin^{M}-Sgg BiFC is also detectable in the squamous epithelium of the peripodial membrane (p), staining at even levels regardless of proximity to Wg-expressing cells; no evidence for trans-luminal signaling is apparent. Wg signaling strength – symmetrical about the Wg-expressing cells (brackets) – is indicated (high, medium and low) (n=10). (I-I″) Magnified views of H, extending from near the band of Wg-expressing cells (brackets in H) to cells exposed to low Wg levels. At intermediate distances from the Wg-expressing cells (corresponding to intermediate Wg levels), Axin^{M}-Sgg BiFC is present in the cytoplasm of the cell body (arrowheads) and in basal regions (white arrows). No significant colocalization of Axin^{M}-Sgg BiFC with α-catenin (red) is detected at adherens junctions (yellow arrows). The image is a maximum intensity projection of a 2.7 μm stack of super-resolution Airyscan images (i.e. about one cell deep). For monochrome images of H, see Fig. S1H. (J) Profiles comparing mean fluorescence intensity of Axin^{M}-Sgg BiFC (green, a.u., arbitrary units) with Dll (blue) across the wing pouch using ImageJ. Data are mean±s.d. (n=7) (a.u., arbitrary units). Scale bars: 20 μm in A,B; 10 μm in D,H,I. See Fig. S6 for context of images. See Table 1 for Pearson's and Manders' correlation coefficients (CCs).

Development (2019) 146, dev164145. doi:10.1242/dev.164145

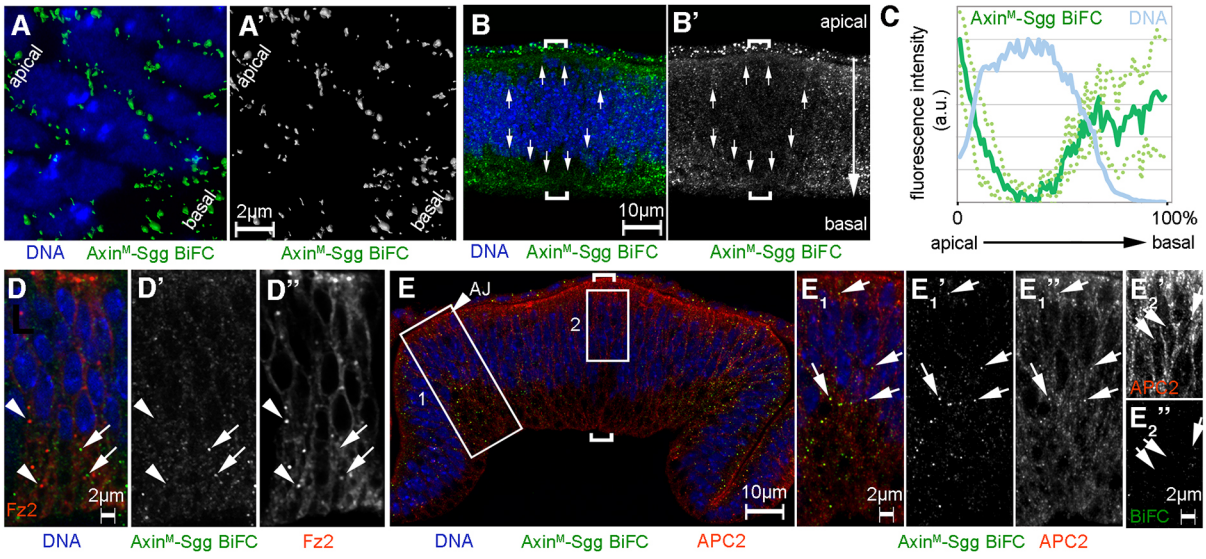

Fig. 2. Axin^{M}-Sgg BiFC objects are cytoplasmic and preferentially depleted the nuclear layer near Wg-secreting cells. (A,A′) A super-resolution Airyscan image processed using Imaris surface-view to reveal Axin^{M}-Sgg BiFC as objects (green), which surround nuclei (blue) in the domain of low Wg signaling (in similar position and orientation to Fig. 1I). The apical and basal extent of the nuclear layer is indicated. This 0.64 µm projection captures only about one-third of the cell diameter; BiFC above and below nuclei is not shown (also see Movie 2). (A′) A monochrome image of the BiFC channel (n=6). (B,B′) Axin^{M}-Sgg BiFC (green, gray in B′) is absent around nuclei (blue) adjacent to Wg-expressing cells (brackets) but BiFC is present in basal and apical cellular regions (arrows), indicating localized signaling around nuclei (n=6) (see Fig. 1E for cell morphology). This z-projection of confocal images is about four cells deep (8.3 µm; enhanced to reveal background). (C) The fluorescence intensity of Axin^{M}-Sgg BiFC (green, arbitrary units) was quantified for regions of interest along the apical-basal axis (see Fig. S2O for illustration). Data are mean±s.d. (n=7). The nuclear position is evident from the blue line (DNA) (mean, n=7). (D-D″) Axin^{M}-Sgg BiFC (green, arrows) does not colocalize with tagged Fz2 (red) in regions of intermediate or low Wg signaling (Fig. 1C), nor do foci of Fz2 colocalize with Axin^{M}-Sgg BiFC (arrowheads), indicating that active DC is predominantly cytoplasmic, not membrane associated. For clarity, tagged Fz2 was clonally induced and boundaries are evident as unstained areas at the left and right of the image in D″ (n=6). (E) Axin^{M}-Sgg BiFC colocalizes with APC2 in lateral regions of the wing pouch (region 1, white arrows); similar foci of APC2 are detected within the domain of strong Wg signaling that do not colocalize with Axin^{M}-Sgg BiFC (region 2, arrows; over-exposed insets in gray scale). The image is a maximum intensity projection of a 0.93 µm stack of super-resolution Airyscan images (i.e. about half a cell deep) (n=6). Scale bars: 10 µm in B,B′,E; 2 µm in all other panels. See Table 1 for Pearson's and Manders' correlation coefficients (CCs). See Fig. S6 for context of images.

altered target gene expression and wing defects), rather than examining signal transduction per se.

Several models suggest that DC activity may be regulated via degradation of a limiting component, which would cause Armadillo to accumulate and activate Wg-dependent gene transcription. Both Axin and GSK3β/Sgg are postulated to function this way (Lee et al., 2003; Taelman et al., 2010; Wang et al., 2016b; Yang et al., 2016), whereby regulation of cytoplasmic levels plays a crucial role in modulating Wg signaling. Accordingly, minor overexpression would prevent signaling. Inconsistent with such a model for Axin, we have shown that an eightfold increase in Axin levels does not reduce Wg signaling as predicted, but instead leaves signaling unaffected (Peterson-Nedry et al., 2008). As an additional test, we expressed tagged versions of Axin, Sgg and APC2 across the Wg gradient using the tubulin-α1 promoter (Peterson-Nedry et al., 2008; see Materials and Methods). Quantification of wing disc expression showed that these proteins were evenly expressed across the Wg gradient (Fig. 1D, Fig. S2B-D). This suggests that Wg signaling does not affect Armadillo stability via the localized degradation of DC components; rather, it suggests that local regulation of DC activity (as opposed to relative abundance of its components) plays a key role in patterning by Wg.

The multifunctional nature of Wg pathway components obstructs direct analysis of Wg signaling mechanisms *in vivo*. Thus, the central regulator of the Wg pathway, the DC, has not been detected by molecular interactions of its components under physiological conditions in living tissue or cells. To overcome this, we use BiFC protocols to visualize the complex. This approach provides an alternative to biochemical methods (often requiring proteins of interest to be expressed at non-physiological levels) and permits visualization of physical protein-protein interactions in a normal cellular context. As shown in Fig. 1F, BiFC takes advantage of the fact that two non-fluorescent fragments of fluorescent protein (here the Venus fragments Ven1 and Ven2) can fold correctly into a fluorophore if brought together in the correct orientation; therefore, incorporating complementary parts of Venus into fusion protein constructs of different DC components allows us to visualize their molecular interactions *in vivo* (Michnick et al., 2007; Robida and Kerppola, 2009). We found that expressing Venus-tagged proteins at functionally relevant expression levels was sufficient to produce detectable BiFC signal (see Materials and Methods). We apply this method to visualize DCs in the wing disc.

First, we determined how expression levels of tubulin-promoter-driven tagged proteins compared with expression of the endogenous proteins (Fig. S1, see Materials and Methods for details about detection and quantification). Western blot analysis revealed that Sgg-Ven1 is expressed at ∼37-fold lower levels than wild-type Sgg [0.027±0.0149 (mean±s.d.); Fig. S1A,E]. In contrast, expression slightly above endogenous protein levels is observed for APC2-Ven1 (∼2.7-fold higher; 2.65±0.95; Fig. S1B,E), Ven2-Axin (∼1.2-fold higher; 1.23±0.67) and Axin^{M}Ven2 (∼1.8-fold higher; 1.84±1.13; Fig. S1C-E). Thus, APC2 and Axin constructs display near-physiological levels of expression, while the Sgg construct is expressed at levels well below the wild-type level.

Next, we tested tagged constructs for functionality and developmental defects. APC2-Ven1 is functional, as it rescues the

Development (2019) 146, dev164145. doi:10.1242/dev.164145

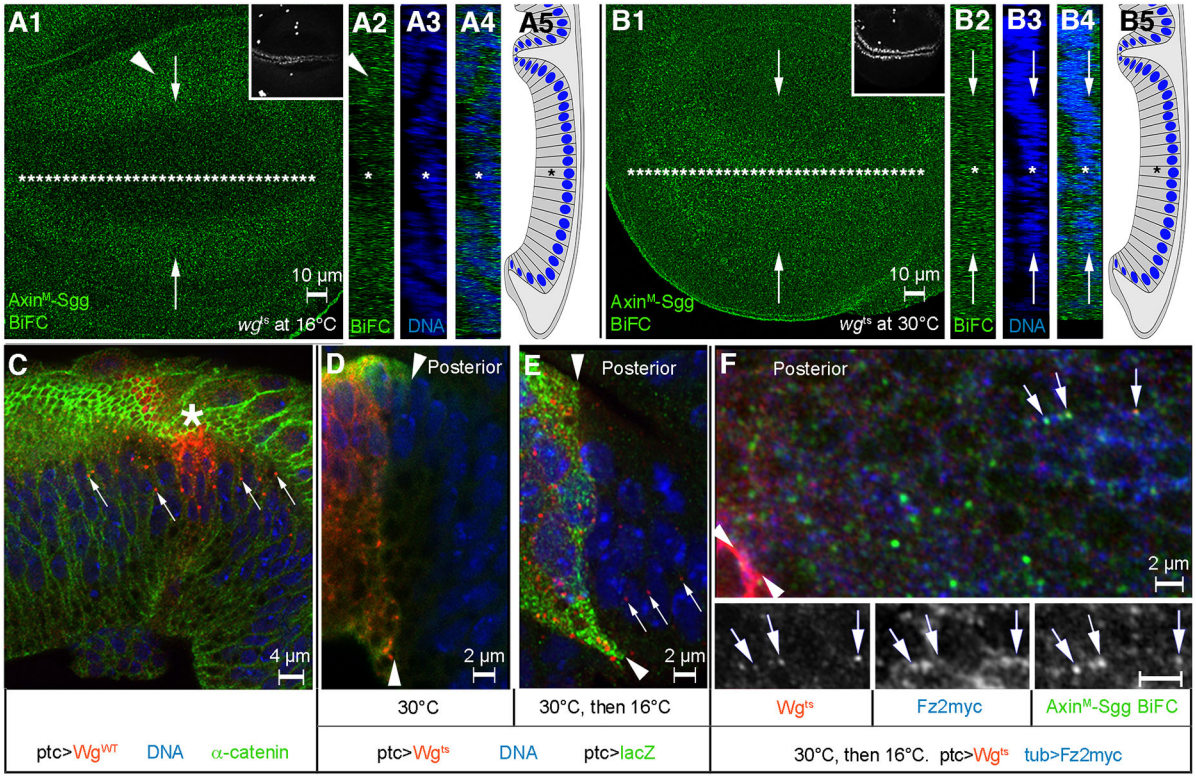

Fig. 3. Changes in Wg signaling induce rapid and dynamic changes in Axin-Sgg BiFC. (A-B5) The wing was imaged as a *z*-stack in top-down view, then subjected to deconvolution. For orientation, the position of Wg-expressing cells is indicated by asterisks (line in A1, B1; single asterisk in A2-A5, B2-B5). Nuclei are in blue to reveal epithelial folding. (A-A4) Axin-Sgg BiFC shows the wild-type pattern of wg^{ts} at 16°C (A1) with low levels about the Wg stripe (asterisks) and higher levels away from it (arrowhead). Computer-generated transverse section of this disc along the white arrows in A1 is shown in A2-4. Epithelial folding is revealed by nuclear stain (blue in A3 and A4; schematically in A5). The folded nature of the pouch precludes detailed observation of low-Wg areas in a top-down view but allows the detection of Sens expression for which a projection is shown (inset in A1). The double line of Senseless expression is Wg dependent (*n*=8). (B-B5) After 50 min of Wg inactivation using temperature-sensitive wg^{ts}, $Axin^{M}$-Sgg BiFC is evident at high levels throughout the wing pouch (B1). A transverse section between the white arrows in B1, shown in B2-B4, shows accumulated $Axin^{M}$-Sgg BiFC in the center of the wing pouch (B2, B4, arrows). Sens expression is not disrupted (B1, inset, projection). BiFC signal in A1-A4 and in B1-B4 was collected using identical settings, except that in B1-B4, signal intensity was 1.7× that of A1-A4, requiring the reduction of laser intensity by 50% to avoid saturating the microscope's detector. Analysis using Imaris software reveals 1.7× more BiFC objects in B1-B4 than in A1-A4 (*n*=8). (C) *ptc*-driven ectopic expression of wild-type Wg (Wg^{WT}; red, asterisk) is detected as Wg foci in adjacent cells (arrows) (*n*=6). (D,E) *ptc*-driven expression of Wg^{ts} is used to 'load' cells at 30°C; co-expressed *lacZ* labels these cells. The posterior boundary of the *ptc* stripe is the anteroposterior (A/P) compartment boundary (arrowheads), which anterior (*ptc*) cells must not cross. Therefore, any Wg^{ts} protein detected in posterior cells must have been secreted (*n*=10). (D) At non-permissive temperature, Wg^{ts} protein is not detected in posterior cells, but upon downshift to permissive temperature (E), secreted Wg^{ts} is readily detectable several cell diameters away (arrows). (F) A 60 min pulse of Wg^{ts} secretion reveals triple colocalization of Wg^{ts} (red), Fz2myc (blue) and Axin-Sgg BiFC (green), indicating translocation of the active DC from the cytoplasm to ligand-activated receptor complexes (arrows; insets show monochrome images). The image was taken in the domain of low-Wg signaling (Fig. 1C2), where $Axin^{M}$-Sgg BiFC is strong (Fig. 1C3,H). Arrowheads indicate the boundary of cells expressing Wg^{ts} (*n*=8). Scale bars: 10 µm in A-A4,B-B4; 4 µm in C; 2 µm in D-F, including insets. See Table 1 for CCs. See Fig. S6 for context of images.

apc apc2 null mutant viability (not shown) and expression in wild type causes no defects (Fig. S2K). We have shown previously that N-terminally tagged Axin fully rescues $axin^{null}$ mutants (Peterson-Nedry et al., 2008) and, accordingly, expression of Ven2-Axin causes no defects in wild-type animals (Fig. S2K, and not shown). Subsequent deletion of a large internal domain between APC- and Sgg-binding sites abolished rescue, yet, surprisingly, embryos were nearly normally patterned, indicating significant retention of function (Peterson-Nedry et al., 2008). Accordingly, the insertion of a tag adjacent to the Sgg-binding site ($Axin^{M}$Ven2) may mildly affect function but the tagged protein would be unlikely to interfere significantly with normal Wg signaling, which is what we observed: $Axin^{M}$Ven2 fails to rescue the $axin^{null}$ mutant, and its ectopic expression during embryogenesis reduces viability, while later expression does not interfere with development (Fig. S2L; not shown). As we wished to assess the ability of Sgg to bind Axin without kinase activity (below), we expressed a catalytically inactive form, Sgg-Ven1, the expression of which caused no developmental defects (Fig. S2L, and not shown). Future experiments will be needed to assess how catalytically active Sgg functions in these assays.

The transduced Wnt signal inactivates DCs by altering the Axin-Sgg interaction

In the active DC, Axin is predicted to bind Sgg (Clevers and Nusse, 2012; Behrens et al., 1998). Prominent models suggest that DC inactivation does not affect the Axin-Sgg association but instead blocks Sgg activity either by kinase inhibition, aggregation of DCs at the activated receptor or functional dissociation of the complex from the ubiquitylation machinery (Piao et al., 2008; Bilic et al., 2007; Li et al., 2012). Therefore, we expected co-expression of tagged Axin and Sgg evenly across the Wg gradient (Fig. 1G, Fig. S2B,D) to produce a uniform BiFC signal. We assessed the ability of several pairs of tagged constructs to generate a BiFC signal

Development (2019) 146, dev164145. doi:10.1242/dev.164145

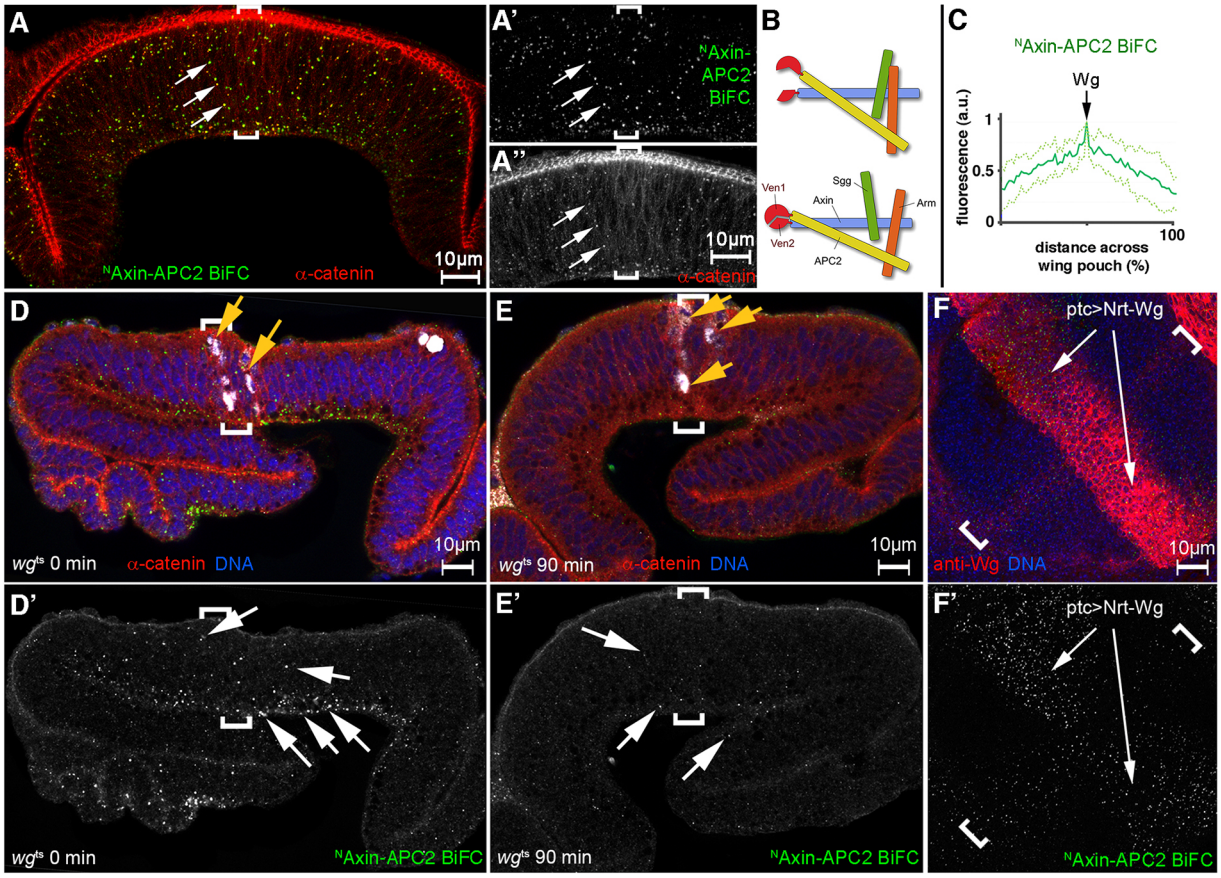

Fig. 4. The ^{N}Axin-APC2 BiFC complex requires sustained Wg signaling. (A-A″) ^{N}Axin-APC2 BiFC is present in a gradient centered about Wg-expressing cells (brackets) in this projection of a 5.7 µm *z*-stack of Airyscan images. (A) Prominent BiFC foci (green) are typically colocalized with α-catenin (A, red; A″, gray, arrows); BiFC foci are also abundant in the basal cytoplasm. (A′,A″) Partial gray scale images of the BiFC signal and α-catenin stain, respectively, shown in A (*n*=12; Table 1). (B) Schematic of the ^{N}Axin-APC2 BiFC complex formed by N-terminally tagged Axin and C-terminally tagged APC2, displaying conformation-specific BiFC. (C) A profile of ^{N}Axin-APC2 BiFC average fluorescence intensity suggests positive regulation by Wg signaling. Data are mean±s.d. (*n*=6). (D,D′) A wild-type pattern of *wg*^{ts} at 16°C displays abundant ^{N}Axin-APC2 foci (green, arrows). The high-Wg target Sens (white, yellow arrows) is induced adjacent to Wg-producing cells (brackets), identifying the position of Wg-expressing cells (*n*=6). (E,E′) Inactivation of Wg signaling for 90 min using temperature-sensitive *wg*^{ts} results in marked reduction of ^{N}Axin-APC2 BiFC foci. Sens expression is maintained during this time (*n*=6). (F,F′) *ptc*>Gal4 driven ectopic expression of Nrt-Wg in the lateral wing disc (red, arrows) induces ectopic ^{N}Axin-APC2 BiFC (green, arrows). White brackets indicate region of endogenous Wg expression. Panels show *z*-projections: a 5.7 µm stack in A-A″, 8 µm stacks for D-F′ (*n*=6). Scale bars: 10 µm. See Fig. S7 for context of images.

in vivo (Fig. S2E). N-terminally tagged Axin (Ven2-^{N}Axin) co-expressed with C-terminally tagged Sgg (Sgg-Ven1) did not produce BiFC (Fig. S2G). This is possibly due to spatial constraints within the DC (Fig. S2F) and underscores the specificity of the BiFC method. When the Ven2 tag was instead inserted near the Sgg-binding site, as it is in Axin^{M}Ven2 with Sgg-Ven1, we observe BiFC (Fig. 1G). Surprisingly, we found that Axin^{M}-Sgg BiFC signal predominated only in regions with low Wg activity (i.e. distant from the Wg stripe and peripheral Wg ring around the pouch; Fig. 1A-C) with gradually declining BiFC signals evident in cells exposed to higher levels of Wg (Figs 1H-J and 2A-C, Fig. S2H-I,M,N). As the Axin^{M}-Sgg interaction is necessary for DC activity and its disruption is sufficient to inactivate the complex (Hedgepeth et al., 1999), our finding identifies this interaction as a key regulatory target in the Wg transduction pathway (Fig. 1G,G′). We consider the Axin^{M}-Sgg BiFC signal indicative of the 'active DC', as its overall distribution matches the distribution predicted for active complex across the Wg gradient (Fig. 1J,C3). If Wg signaling indirectly regulates Wg-target gene expression by depleting active DC, then the gradient of active DC (Axin^{M}-Sgg BiFC) should correspond to an inverse gradient of Dll, as is observed (Fig. 1J, Fig. S2M). Curiously, Axin^{M}-Sgg BiFC decreases towards the edge of the pouch. This may be due to Wg from the ring of expressing cells surrounding the wing pouch (see Fig. 1A-C).

Axin^{M}-Sgg BiFC is reduced in the nuclear layer in response to signaling

Activation of target gene transcription by Armadillo represents the final event in Wg signal transduction. Armadillo must enter the nucleus from the cytoplasm, suggesting that this region of the cell is crucial for DC activity. Airyscan super-resolution confocal microscopy showed Axin^{M}-Sgg BiFC objects throughout the cytoplasm of the cell body. BiFC signal was detected in apical and basal regions of cells (arrows in Fig. 1I, see also Fig. 2A, Fig. S2H,M) as well as surrounding nuclei in the domain of minimal Wg signaling (arrowheads in Figs 1I and 2A, Movies 1 and 2). Strikingly, while levels of Axin^{M}-Sgg BiFC remained high in basal and apical regions of the cytoplasm near Wg-expressing cells, BiFC signal was either absent or greatly reduced in the nuclear layer (white arrows, Fig. 2B,C, Fig. S2O, see also Fig. 1E). This indicates that stronger signaling leads to localized inactivation of the DC within the nuclear layer of the epithelium (arrows, Fig. 2B,

Development (2019) 146, dev164145. doi:10.1242/dev.164145

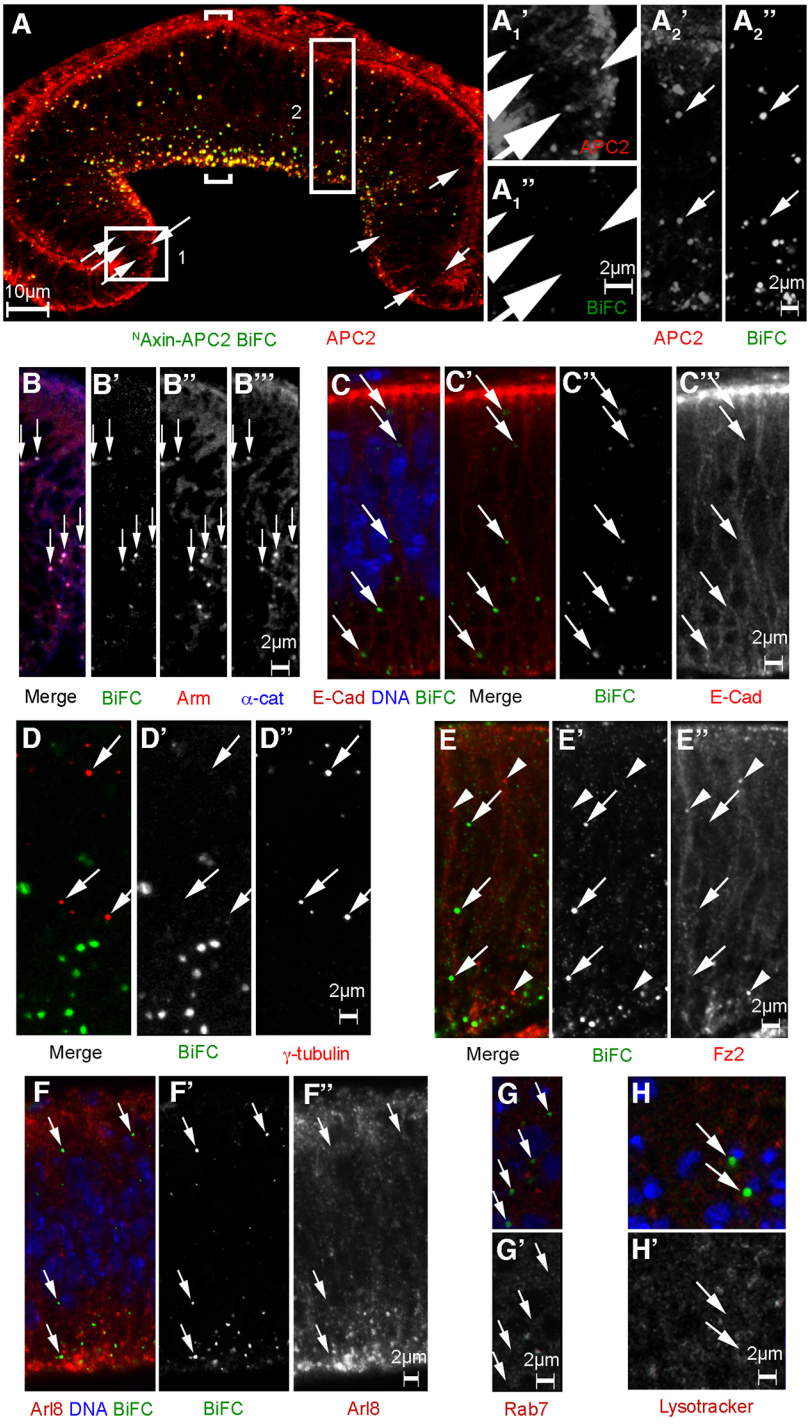

Fig. 5. Visualization of inactivated DC *in vivo*. (A-A_2'') APC2 foci (red) are not limited to the ^{N}Axin-APC2 complex adjacent to the Wg signaling domain (brackets and region 2, A_2',A_2'') but are also found in more-lateral regions of weak Wg signaling with no ^{N}Axin-APC2 BiFC colocalization (region 1, A_1',A_1''; arrows; compare with Fig. 2E, Fig. S2I) (n=6; Table 1). (B-B‴) ^{N}Axin-APC2 BiFC foci (B′) colocalize with Armadillo (B″) and α-catenin (B‴). Triple colocalization is detected for ^{N}Axin-APC2 BiFC with Armadillo and α-catenin (n=6; Table 1). (C-C‴) ^{N}Axin-APC2 BiFC foci (C″) do not colocalize with E-Cadherin (C‴) (n=6; Table 1). (D-D″) ^{N}Axin-APC2 BiFC foci (D′) do not colocalize with centrosomal marker γ-tubulin (D″, arrows; n=6; Table 1). (E-E″) ^{N}Axin-APC2 BiFC foci (E′; arrows) do not colocalize with Fz2myc (E″), nor do Fz2myc foci colocalize with BiFC (arrowheads; Table 1) (n=10). (F-F″) ^{N}Axin-APC2 BiFC foci (F′) do not colocalize with multivesicular endosome marker Arl8 (F″). (G,G′) Rab7 (red, G′) does not colocalize with ^{N}Axin-APC2 BiFC foci (green, arrows; n=6). (H,H′) Lysotracker (red) does not colocalize with ^{N}Axin-APC2 BiFC foci (arrows, green) (n=6; Table 1). Each panel shows a single confocal section. High-magnification images (B-H) are from the domain of strong Wg signaling (see Fig. 1C2) and are enhanced to reveal background. A-F (transverse cryosections) show the epithelium from apical (top) to basal, and G,H show top-down views. Scale bar: 10 μm in A; 2 μm in all other panels. See Table 1 for CCs. See Fig. S7 for context of images.

Movie 3). Indeed, the distribution of intracellular Wg supports this notion, as it predominates in the nuclear layer of the epithelium (Fig. S2N).

Axin^{M}-Sgg BiFC is primarily cytoplasmic

DC components are cytoplasmic proteins and some models postulate that active DC resides in the vicinity of Wg receptor complexes at the membrane (e.g. Tolwinski, 2009; Bilic et al., 2007; Wang et al., 2016a; Davidson et al., 2005). A comparison of Axin^{M}-Sgg BiFC with Frizzled2 (Fz2, a component of Wg receptors) revealed little or no colocalization in the juxtamembrane region with super-resolution microscopy, indicating that most active DC resides away from Fz2 receptors (Fig. 2D, Table 1). Table 1 lists Pearson's and Manders' correlation coefficients (CCs) for original images. CCs may be affected by the relative abundance of proteins. For example, specific colocalization with a small fraction of a highly abundant protein may yield a low Manders' CC. Spurious and specific colocalization can be distinguished by shifting or rotating one channel relative to the other: if the resulting CC is significantly lower, then colocalization was likely meaningful, whereas an insignificant change in CC indicates insignificant co-localization (McDonald and Dunn, 2013; Adler and Parmryd, 2010; Dunn et al., 2011). We verified the validity of CCs by shifting one channel and the data are shown in Table 1 (see also Materials and Methods).

Development (2019) 146, dev164145. doi:10.1242/dev.164145

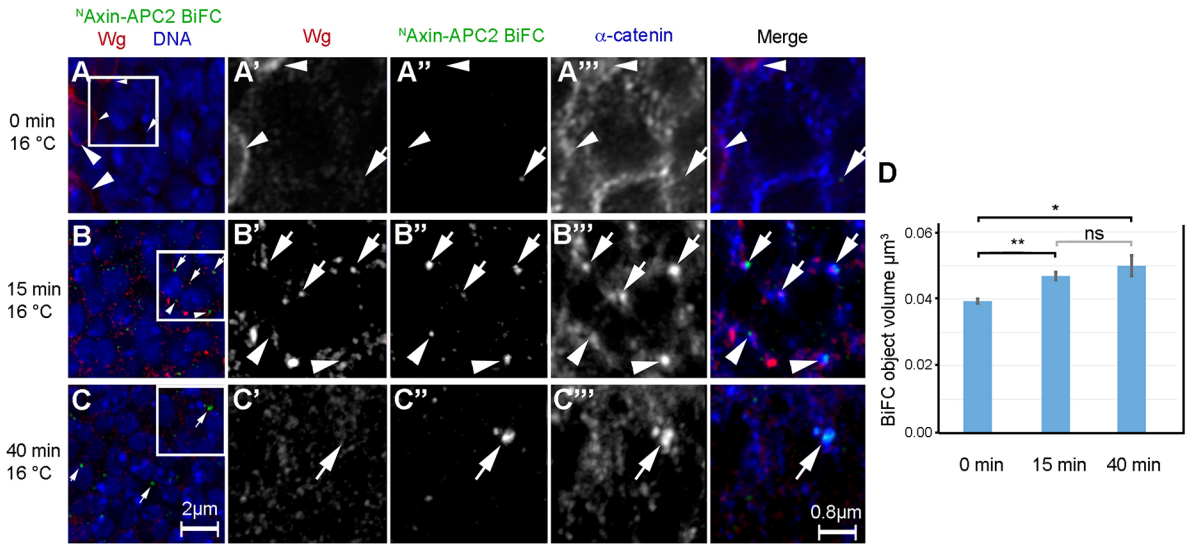

Fig. 6. Pulsed Wg signaling *in vivo* reveals the dynamics of DC inactivation and translocation. A pulse of ectopic Wg expression was induced in the domain of low Wg signaling within the wing pouch of flies expressing Ven2-^{N}Axin+APC2-Ven1 (see Materials and Methods; Fig. 1C2, Fig. S3). (A-A‴) After 0 min., Wg^{ts} is detected in Wg-producing cells in the *ptc* stripe (arrowheads in A,A′); sporadic ^{N}Axin-APC2 BiFC foci are detected (A″, arrow), possibly resulting from BiFC formation between two DCs (*n*=6; Table 1). (B-B‴) After 15 min, Wg^{ts} colocalizes with newly induced ^{N}Axin-APC2 BiFC and α-catenin (arrows in B′-B‴; Table 1), although some foci have little or no detectable α-catenin (not shown). Foci of Wg^{ts} and BiFC are frequently observed in close proximity, albeit without colocalization (arrowheads). The association of Wg^{ts} with ^{N}Axin-APC2 BiFC is transient and not detected at 40 min (C) (*n*=6; Table 1). (C-C‴) At 40 min, foci of colocalizing BiFC and α-catenin appear larger (arrows in C″,C‴). This colocalization of inactivated DC with α-catenin is characteristic of cells in a steady-state signaling environment, as shown Fig. 4A. Colocalization of BiFC with Wg is no longer detected (arrows, C′,C″; Table 1). Merged images are shown with DNA stained blue in the left-most column. Insets are shown in gray scale and merge, with α-catenin in blue in the right-most column. Images are shown with enhanced background for context. Results were observed in six wing discs each. Representative images are shown (*n*=7). (D) Range of volumes of BiFC objects in response to Wg^{ts} signaling at 0 min, 15 min and 40 min (data are mean±s.e.m.). A significant difference was detected between 0 min and 15 min (**$P<1.5\times10^{-7}$; *t*-test, two-tail) and 0 min and 40 min time points (*$P<0.001$; *t*-test, two-tail), but not between 15 min and 40 min (ns, $P\geq0.37$; *t*-test, two-tail). Scale bars: 2 μm; 0.8 μm in magnified insets. See Fig. S7 for context of images and Table 1 for CCs.

Axin-Sgg BiFC colocalizes with a subpopulation of APC2

APC is an essential component of the DC that also functions in cell adhesion, migration and mitosis (McCartney and Peifer, 2003). Therefore, we anticipated widespread APC staining, wherein a subset of APC would colocalize with DC. Indeed, all Axin^{M}-Sgg BiFC colocalized with APC2 (Fig. 2E, region 1; Table 1). In cells with strong Wg signaling, a distinct APC2 subpopulation was evident as cytoplasmic foci that did not colocalize with Axin^{M}-Sgg BiFC (Fig. 2E, region 2; Table 1), presumably serving other functions. Similarly, adherens junctions contain APC2 (Fig. 2E) and α-catenin (yellow arrows, Fig. 1I; Fig. S2H) but lack Axin^{M}-Sgg BiFC signal (Table 1).

Axin^{M}-Sgg BiFC rapidly accumulates in response to disrupted Wg signaling

Our findings suggest that Axin^{M}-Sgg BiFC complexes are negatively regulated by the endogenous Wg gradient (Figs 1 and 3A). Therefore, we expected loss of Wg signaling to permit accumulation of Axin^{M}-Sgg BiFC in regions where it is normally absent (e.g. disc regions with high endogenous Wg levels; Fig. 1C). A temperature-sensitive allele of Wg (*wg*^{ts}; Materials and Methods) contains the Cys104Ser mutation, which renders Wg^{ts} secretion-deficient at non-permissive temperature (30°C; González et al., 1991; van den Heuvel et al., 1993). We found that when *wg*^{ts} larvae were incubated at 30°C to disrupt signaling for 50 min, Axin^{M}-Sgg BiFC was significantly induced at the center of the wing pouch (Fig. 3B, Fig. S3G). Thus, loss of Wg signaling is sufficient for accumulation of active DC in regions where it is normally absent.

Previous studies show that the Wg-target Senseless (Sens) requires high Wg levels and is induced only adjacent to Wg-expressing cells (Jafar-Nejad et al., 2006). Prolonged loss of Wg signaling leads to reduced Sens expression (Jafar-Nejad et al., 2003). When we inhibited Wg signaling by shifting *wg*^{ts} flies to the non-permissive temperature, we still detected normal Sens expression after 50 min (Fig. 3B1, inset), while Axin^{M}-Sgg BiFC levels were substantially increased in these regions (Fig. 3A,B, Fig. S3G; Materials and Methods). Only prolonged inactivation of Wg signaling (>4 h) substantially diminished Sens expression (not shown), demonstrating that the increase in Axin^{M}-Sgg BiFC signal represents the earliest molecular indicator of altered Wg signaling *in vivo* identified to date, preceding subsequent changes in Wg target gene expression.

Conversely, we predicted that the induction of ectopic Wg signaling might abolish Axin^{M}-Sgg BiFC complexes normally present in regions with low endogenous Wg levels. Expression of wild-type Wg in the pattern of *ptc*, which runs perpendicular to the Wg gradient, yielded ectopic Wg ligand (Fig. 3C, Fig. S3A-C). In contrast to prolonged expression of Wg, a pulse of signaling might result in synchronized signaling and an increase in the relative abundance of early transient events that lead to DC inactivation. We again took advantage of Wg^{ts}. For ease of detection of Wg^{ts} secretion, we focused on non-expressing cells adjacent to the *ptc*-stripe. No Wg^{ts} secretion was detected at non-permissive temperature (30°C; Fig. 3D) but after shifting to permissive temperature (16°C) for 15 min, Wg^{ts} protein was detected several cell diameters away (Fig. 3E). This rapid response indicates no *de novo* synthesis of Wg^{ts} protein is required, consistent with previous reports (González et al., 1991; van den Heuvel et al., 1993). In this way, we were able to 'load' cells with inactive Wg^{ts} by culturing larvae at non-permissive temperature and then release a pulse of

Development (2019) 146, dev164145. doi:10.1242/dev.164145

Table 1. Pearson's and Manders' correlation coefficients

Figure	PCC	PCC (control channel shift)	MCC	MCC (control channel shift)	MCC	MCC (control channel shift)	BiFC colocalization partner
1I	PCC=0.0879	0.0020	MCC (BiFC)=0.3867	0.3867	MCC (α-catenin)=0.0551	0.0343	α-Catenin
2D	PCC=0.0309	0.0051	MCC (BiFC)=0.5630	0.5630	MCC (Fz2)=0.1092	0.0712	Fz2
2E	PCC=0.4869	0.1563	MCC (BiFC)=0.2233	0.0003	MCC (APC2)=0.0643	0.0003	APC2 (Region 1)
	PCC=−0.0654	0.4526	MCC (BiFC)=0.0166	0.0008	MCC (APC2)=0.0023	0.0166	APC2 (Region 2)
3F	PCC=0.0937	0.0045	MCC (BiFC)=0.8870	0.8870	MCC (Fz2)=0.0343	0.0237	Wg
	PCC=0.0118	−0.0254	MCC (BiFC)=0.8870	0.8870	MCC (Wg)=0.0243	0.0182	Fz2
	PCC=0.1002	0.0412	MCC (BiFC)=0.8891	0.8886	MCC (Wg, Fz2)=0.0885	0.0272	BiFC, Wg and Fz2 triple colocalization
4A	PCC=0.4971	−0.0219	MCC (BiFC)=0.1824	0.1830	MCC (α-catenin)=0.0261	0.0077	α-Catenin
5A	PCC=0.4710	−0.1107	MCC (BiFC)=0.4327	0.4471	MCC (APC2)=0.0849	0.0042	APC2
5B	PCC=0.6545	−0.1198	MCC (BiFC)=0.1070	0.1089	MCC (APC2)=0.0862	0.0092	Armadillo
	PCC=0.5428	−0.0675	MCC (BiFC)=0.1070	0.1115	MCC (Armadillo)=0.0694	0.0113	α-Catenin
	PCC=0.6051	0.0000	MCC (BiFC, α-catenin)=0.5502	0.0000	MCC (Armadillo)=0.1070	0.0000	BiFC, α-catenin and Armadillo triple colocalization
5C	PCC=−0.1181	0.0262	MCC (BiFC)=0.1232	0.1237	MCC (E-Cadherin)=0.0018	0.0020	E-Cadherin
5D	PCC=0.0389	−0.1665	MCC (BiFC)=0.0089	0.0087	MCC (γ-tubulin)=0.0015	0.0010	γ-Tubulin
5E	PCC=−0.0141	0.0647	MCC (BiFC)=0.0041	0.0034	MCC (Fz2)=0.2183	0.2186	Fz2
5F	PCC=−0.0581	−0.0325	MCC (BiFC)=0.1027	0.1036	MCC (Arl8)=0.0112	0.0074	Arl8
5G	PCC=−0.1027	0.0143	MCC (BiFC)=0.0260	0.0262	MCC (Rab7)=0.2636	0.2644	Rab7
5H	PCC=−0.1753	−0.1591	MCC (BiFC)=0.0024	0.0034	MCC (Lysotracker)=0.0469	0.0481	Lysotracker
6A	PCC=0.0288	0.0188	MCC (BiFC)=0.3629	0.3624	MCC (Wg)=0.0458	0.0383	Wg
	PCC=0.1099	0.0410	MCC (BiFC)=0.3629	0.3624	MCC (α-catenin)=0.0527	0.0409	α-catenin
6B	PCC=0.0580	0.0202	MCC (BiFC)=0.3360	0.3373	MCC (Wg)=0.0535	0.0484	Wg
	PCC=0.3348	0.0438	MCC (BiFC)=0.3360	0.3373	MCC (α-catenin)=0.0784	0.0493	α-catenin
6C	PCC=−0.0109	−0.0429	MCC (BiFC)=0.1215	0.2414	MCC (α-catenin)=0.0041	0.0166	Wg
	PCC=0.4239	−0.0203	MCC (BiFC)=0.1215	0.2414	MCC (Wg)=0.0315	0.0184	α-catenin

BiFC, bimolecular fluorescence complementation; PCC, Pearson's correlation coefficient; MCC, thresholded Manders' correlation coefficient.
To determine CCs for triple colocalization, a colocalization mask was created for two channels, which was then used to determine the extent of colocalization with the third channel. PCC and MCC control values were obtained by shifting one channel, which is expected to abolish meaningful co-localization.

active Wg^{ts} by shifting to permissive temperature (Fig. 3D-E, Fig. S3A,D,E; Materials and Methods; Couso et al., 1994). Foci of ectopic Wg^{ts} colocalized with Fz2 after 30 min of pulse initiation (Fig. S3F), indicating likely receptor activation. As shown in Fig. 2D, $Axin^{M}$-Sgg BiFC was generally found to be cytoplasmic, with little or no colocalization with Fz2 foci in a stable signaling environment. However, 60 min after the induction of ectopic Wg secretion, triple colocalization of Wg^{ts}, Fz2 and $Axin^{M}$-Sgg BiFC was detected, representing the first demonstration of DC translocation to ligand-bound receptor complexes (Fig. 3F).

^{N}Axin-APC2 BiFC reports the conformation of inactivated DCs

Next, we examined whether BiFC could be used to detect Axin-APC interactions. DC activity depends on APC (Clevers and Nusse, 2012; Spink et al., 2000) and, as expected, APC2 colocalized with $Axin^{M}$-Sgg BiFC (Fig. 2E). However, whether inactivated DCs also contain APC remains controversial (Li et al., 2012; Valvezan et al., 2012). Accordingly, we tested a panel of different BiFC reporter constructs of Axin and APC2 to address this issue (Materials and Methods; Fig. S2E). BiFC was detected between N-terminally tagged Ven2-Axin and C-terminally tagged APC2-Ven1 (Fig. 4A-B). Unexpectedly, ^{N}Axin-APC2 BiFC signals appeared to be positively regulated by Wg signaling, indicated by bright ^{N}Axin-APC2 BiFC foci that are present in a gradient centered on Wg-expressing cells (Fig. 4C). This distribution follows the pattern of Wg signaling gradient (Fig. 1C2), which induces DC inactivation; it is complementary to the distribution of active DC ($Axin^{M}$-Sgg BiFC; Fig. 1C3,J). Thus, only a subpopulation of DCs displayed ^{N}Axin-APC2 BiFC. These results suggest that while Axin and APC2 are present in both the inactivated and active DCs, the conformation yielding ^{N}Axin-APC2 BiFC signal dominates in cells with inactivated DC, where it is induced by Wg signaling (Fig. 4C). ^{N}Axin-APC2 BiFC foci were present in the part of the cytoplasm located in the nuclear layer where we expect signaling to occur. However, some accumulation in the basal cytoplasm was also evident (Figs. 4A,D and 5A,D-F, Movie 4). Variation in apical-basal position occurred within and between discs; its cause will require further investigation. In the domain of strong Wg signaling, an average of only about one to two relatively large ^{N}Axin-APC2 BiFC objects per cell were evident (1.45±0.48; Fig. S4C-G), contrasting with an order of magnitude more abundant $Axin^{M}$-Sgg BiFC foci per cell in the domain of minimal Wg signaling (Fig. S4G; 29.51±10.46; $P<0.0005$). As the more abundant $Axin^{M}$-Sgg BiFC foci were of smaller apparent size than ^{N}Axin-APC2 BiFC objects, we estimated their apparent size with image analysis software (Imaris), using fluorescence intensity as a proxy for size (Fig. S4H,I; Materials and Methods). The apparent mean diameter for $Axin^{M}$-Sgg BiFC objects is 0.26 µm (±0.08; $n=213$) and 0.58 µm (±0.10; $n=96$) for ^{N}Axin-APC2 BiFC objects representing a significant difference ($P<3\times10^{-93}$). Assuming spherical shape, one ^{N}Axin-APC2 BiFC object may accommodate the combined volume of about ten $Axin^{M}$-Sgg BiFC objects (Fig. S4I). For these reasons, we consider these large ^{N}Axin-APC2 BiFC foci to be super-complexes of inactivated DCs.

The distribution of ^{N}Axin-APC2 BiFC signals in the wing disc suggests Wg signaling induces DC inactivation concomitant with induction of BiFC (Fig. 4). Therefore, loss of Wg signaling should result in loss of ^{N}Axin-APC2 BiFC. When we inactivated endogenous Wg signaling for 90 min (using temperature-sensitive wg^{ts}), we observed greatly reduced levels of ^{N}Axin-APC2 BiFC (Fig. 4D,E). In contrast, expression of Sens (a high-threshold marker for Wg signaling) was maintained during this period (Fig. 4D-E; yellow arrows, gray scale in merge). In this context,

Development (2019) 146, dev164145. doi:10.1242/dev.164145

^{N}Axin-APC2 BiFC functions as a rapid reporter for changes in Wg signaling, preceding transcription-dependent changes in cell fate determination that are regulated by Wg. Prolonged inactivation of Wg expression (over 24 h, using the wg^{ts} allele) abolished both ^{N}Axin-APC2 BiFC and Sens expression (Fig. S5). Conversely, when we induced a band of localized ectopic Wg expression orthogonal to endogenous Wg (using *ptc*>Gal4 to drive expression of Wg) fused to the transmembrane protein Nrt (Nrt-Wg; Fig. S3A; Zecca et al., 1996), we detected ^{N}Axin-APC2 BiFC associated with ectopic Wg signaling (Fig. 4F). This provides further evidence that ^{N}Axin-APC2 BiFC signal is induced by Wg-dependent changes in the DC, which are associated with rapid inactivation.

As anticipated, APC2 was present in ^{N}Axin-APC2 BiFC foci (Fig. 5A, Table 1), as well as in the domain of low Wg signaling (Figs 1C and 5A, Table 1), consistent with the pattern of $Axin^{M}$-Sgg BiFC signals (Figs 1H,I and 2A,E, Table 1). As inactivated DC is unable to turn over Armadillo, some accumulation of the protein at the inactivated DC is expected (Li et al., 2012; Gerlach et al., 2014). Indeed, the ^{N}Axin-APC2 BiFC foci colocalized with foci of both α-catenin and Armadillo (Figs 4A and 5B, Table 1). Such foci of α-catenin have been previously reported (Somorjai and Martinez-Arias, 2008) but appear more pronounced upon expression of ^{N}Axin-APC2 BiFC transgenes. This observation provided an opportunity to evaluate the effect of BiFC on α-catenin foci. The fluorescence intensity of α-catenin foci was compared between the anterior and posterior wing pouch by limiting ^{N}Axin-APC2 BiFC transgene expression to the posterior compartment. The fluorescence intensity of α-catenin foci was increased by 25% if ^{N}Axin-APC2 BiFC constructs were expressed (Fig. S4A,B), indicating that while expression of BiFC complex modestly affected endogenous complexes, our near-physiological expression of BiFC constructs does not cause artefactual aggregation of DC components.

We also investigated whether ^{N}Axin-APC2 BiFC signals overlapped with other subpopulations of APC known to serve non-signaling purposes. APC proteins function in adhesion and are associated with adherens junctions, where they colocalize with Cadherin (McCartney and Peifer, 2003). However, we detected no colocalization of ^{N}Axin-APC2 BiFC with E-Cadherin at adherens junctions (Fig. 5C, Table 1). APC proteins are also associated with the centrosome, where they function in mitosis (McCartney and Peifer, 2003). As with E-Cadherin, we detected no colocalization of ^{N}Axin-APC2 BiFC with γ-tubulin: a centrosomal marker (Fig. 5D, Table 1). These results support our hypothesis that ^{N}Axin-APC2 BiFC signals are specifically produced by inactivated DCs.

Some prominent models of Wnt signaling postulate that activated Wnt receptors cluster together and subsequently induce aggregates of active DC, causing DC inactivation that depends on prolonged interaction of Wnt receptor and DCs (Bilic et al., 2007; Li et al., 2012; Piao et al., 2008; Roberts et al., 2011; Schwarz-Romond et al., 2007b; Schwarz-Romond et al., 2007a). We therefore tested whether inactivated complexes (revealed by ^{N}Axin-APC2 BiFC) colocalized at the membrane with epitope-tagged Fz2. However, many ^{N}Axin-APC2 BiFC foci were localized in basal cytoplasmic regions with only a few juxta-membrane BiFC foci in the region of the nuclear layer (Fig. 5E, arrows; Table 1), arguing against such a model.

Alternatively, DC inactivation may occur through its removal from the cytoplasm and trafficking into multivesicular endosomes (MVE; Taelman et al., 2010). However, no colocalization of ^{N}Axin-APC2 BiFC was detected with the MVE compartment marker Arl8 (Fig. 5F, Table 1; Rosa-Ferreira and Munro, 2011). Trafficking to the MVE is also thought to require Rab7, yet no colocalization of ^{N}Axin-APC2 BiFC and Rab7 was detected (Fig. 5G, Table 1). Disruption of trafficking to MVE by RNAi knockdown of Vps16 (Pulipparacharuvil et al., 2005) also did not cause the accumulation of ^{N}Axin-APC2 in vesicles (not shown). In addition, labeling lysosomes and associated components of the endocytic pathway with Lysotracker revealed no colocalization with ^{N}Axin-APC2 BiFC (Fig. 5H, Table 1). In summary, the ^{N}Axin-APC2 BiFC complex is absent from MVE and endolysosomal compartments but instead is present in large cytoplasmic complexes, where few are in juxtamembrane positions in the nuclear layer.

Pulsed Wg signaling reveals dynamic changes in DC conformation and localization

The initial events of Wnt signaling triggered by receptor activation might be relatively short-lived. Under steady-state conditions, signaling may be subject to feedback interactions, which may obscure these short-lived events. To address this issue, we used Wg^{ts} mutant protein to release a Wg pulse and imaged the developing wing pouch after 0 min, 15 min or 40 min of Wg secretion (as described above for *ptc*-Gal4 driven Wg^{ts} expression; Fig. 3C-E, Fig. S3A-E). Changes in signaling would be most evident in the region of low Wg signaling (Fig. 1C), where ^{N}Axin-APC2 BiFC is normally absent, and early signaling events in responding cells become evident as newly induced ^{N}Axin-APC2 BiFC.

Prior to Wg secretion, ^{N}Axin-APC2 BiFC was at background levels. Notably, when Wg was secreted for 15 min, colocalization of newly formed ^{N}Axin-APC2 BiFC signal with Wg became evident (Fig. 6A,B, Table 1). As these BiFC signals report the inactivated DC, this represents the earliest functionally significant event reported for the Wnt signaling pathway. Foci of colocalization by Wg and ^{N}Axin-APC2 BiFC were infrequent, consistent with short-lived transient events. While some of these foci colocalized with α-catenin, a subpopulation of these showed no α-catenin colocalization (Fig. 6B, Table 1). Strikingly, 40 min after pulsed Wg expression, the ^{N}Axin-APC2 BiFC complexes no longer colocalized with Wg but instead colocalized with α-catenin (Fig. 6C, Table 1). These results highlight the fact that the initial steps in Wg signaling involve different protein-protein interactions than can usually be demonstrated under steady-state conditions, which may explain discrepancies that have been reported in other studies.

DISCUSSION

BiFC reveals active and inactivated DCs *in vivo*

We demonstrated that BiFC methods using near-physiological protein expression levels are able to resolve specific protein-protein interactions as they occur during Wg pathway activation *in vivo*. The specificity of this method is underscored by the different outcomes observed with combinations of BiFC reagents: some construct pairs lack detectable BiFC (Fig. S2G) whereas others yield BiFC patterns regulated by long-range signaling (Figs 1–6). We detected β-catenin DCs *in vivo* by their molecular interactions and identified their subcellular location and dynamics through a combination of BiFC-based detection methods, cryosectioning and pulsed Wnt signaling. By focusing on the molecular interactions between Axin, Sgg and APC2, we were able to visualize both active and inactivated DCs in the context of an endogenous Wnt gradient, providing a spatial and temporal framework for *Drosophila* Wnt signaling (Fig. 7). We were surprised to find that BiFC detects conformational differences within protein complexes, a degree of sensitivity difficult to attain with *in vivo* methods (Figs 1G and 4B). Previous studies relied on *in vitro* biochemical experiments to investigate molecular

Development (2019) 146, dev164145. doi:10.1242/dev.164145

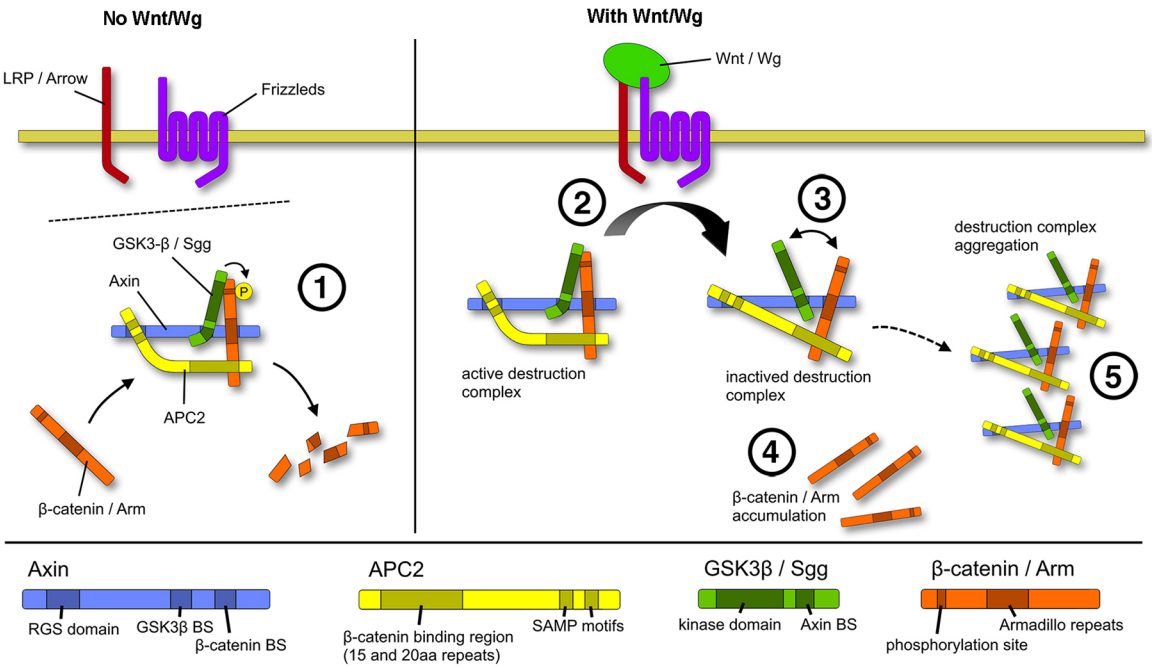

Fig. 7. Dynamics of Wnt signal transduction. (1) In the absence of Wnt, cytoplasmic DC actively targets Armadillo/β-catenin for destruction, thereby preventing activation of the Wnt transduction pathway. (2) Ligand-dependent activation of Wnt receptor (Frizzled-Arrow/LRP complexes) induces translocation of DC to activated receptors. (3) Conformational changes within the DC disrupt Axin-Sgg/GSK3β interactions, rendering the complex inactive. (4) Armadillo/β-catenin accumulates and engages in nuclear signaling. (5) Inactivated DC is assembled into large cytoplasmic super-complexes that become saturated with α-catenin (not shown) and Armadillo (β-catenin). These complexes are subsequently moved out of the cytoplasm from the cell body towards basal regions. This conformation predominates under steady-state conditions and is maintained by continuous signaling.

interactions among DC components, but most of these methods required overexpression protocols and only evaluated Wnt signaling at steady-state without real cellular context. By revealing dynamic interactions between Wnt pathway components *in vivo*, our approach provides an entirely new perspective on Wnt signaling. Therefore, these BiFC-based methods reported herein to investigate Wnt signaling also provide a new paradigm for investigating the dynamic regulation of other signaling pathways *in vivo*.

DC activity controls β-catenin near the nucleus

We found that active DCs, revealed by Axin^{M}-Sgg BiFC, were predominantly cytoplasmic and maximally present in cells with minimal Wg signaling (Figs 1H-J and 2A,E). We infer that localization of active DC around the nucleus plays a principal role in preventing β-catenin from entering the nucleus. As cells are exposed to higher concentrations of Wg, active DCs become less frequent, disappearing entirely in cells exposed to maximal Wg signaling (Fig. 2B,C). Interestingly, cells in intermediate positions display active DC in apical and basal regions, indicating constitutive assembly of the complex, but are depleted of active DC in the cytoplasm in the nuclear layer (Fig. 2B,C). This non-uniform response suggests signaling is localized to the nuclear layer of the epithelium, with concomitant accumulation of endocytosed Wg (Figs 1E and 2A-C, Fig. S2N). Similar observations of localized or asymmetric Wnt signaling have been reported for mammalian stem cells *in vitro* and cell fate determination in the *C. elegans* embryo (Sugioka et al., 2011; Habib et al., 2013). In both instances, localized Wnt receptor activation restricts signaling to only part of the cell. It occurs in the context of asymmetric cell division and restricts nuclear β-catenin accumulation to one of the two nuclei before completion of mitosis. Currently, there is no evidence for Wnt-dependent asymmetric divisions in the patterning of the wing disc.

Conformational changes inactivating DCs are induced during transient interactions with the ligand-activated receptor

Active DCs are predominantly cytoplasmic and do not colocalize with Fz2 receptors at steady state. However, active DCs and ligand-activated receptors rapidly colocalize upon induced signaling (by a pulse of Wg; Fig. 3F, Fig. S3F, Fig. 6B), suggesting that DC translocation to the membrane is initiated by an unrecognized signal originating from the activated receptor and precedes DC inactivation and β-catenin/Armadillo signaling.

Active DCs, revealed by Axin^{M}-Sgg BiFC, decline gradually in cells exposed to more Wg ligand, indicating that Wg signaling inhibits interactions between Sgg and Axin, a finding that is both unexpected and significant (Figs 1H-J and 2B,C, Fig. S2H,M). As Sgg/GSK3β must be bound to Axin for full DC activity (Hedgepeth et al., 1999), the discovery that Wg signaling disrupts this interaction provides a novel mechanistic model for how the catalytic activity of the complex is rapidly downregulated by the presence of Wnt ligand. In addition, once the DC becomes inactivated, its components assume a new conformation that can be detected as ^{N}Axin-APC2 BiFC. The physical interaction of Axin with the Wnt co-receptor LRP5/LRP6 (Arrow, in *Drosophila*; Mao et al., 2001, Tolwinski et al., 2003) depends on phosphorylation of LRP5/LRP6/Arrow by GSK3β/Sgg (Zhang et al., 2006; Zeng et al., 2008; Davidson et al., 2005; Bilic et al., 2007; Cliffe et al., 2003; Piao et al., 2008). It is tempting to speculate that the interaction between Axin and GSK3β/Sgg is disrupted and induces the conformational change because GSK3β/Sgg binds substrate sites on LRP5/LRP6/Arrow. This conformational change then allows for BiFC between Axin and APC2 (schematically illustrated in Figs 4B and 7). Two binding sites for APC on Axin have been identified (Behrens et al., 1998; Ikeda et al., 1998; Pronobis et al., 2015). It remains to be determined whether these differing binding sites are

Development (2019) 146, dev164145. doi:10.1242/dev.164145

required for intramolecular ^{N}Axin-APC2 BiFC or whether intermolecular BiFC occurs as inactivated DC aggregate into super-complexes, as has been proposed (Schaefer et al., 2018; Schaefer and Peifer, 2019).

While conformational changes inactivate the complex, Sgg/GSK3β may still remain associated with the Axin complex (Gerlach et al., 2014; Li et al., 2012). Following disruption of the Axin-Sgg/GSK3β interaction in response to Wg stimulation, the inactivated DC dissociates from the receptor. It colocalizes with α-catenin and β-catenin, as we observed at steady state. Such colocalization is significant because it is consistent with an inactivated DC that binds but does not catalytically turn over β-catenin (Gerlach et al., 2014; Li et al., 2012). In contrast, we did not detect colocalization of Armadillo or α-catenin with the active DC. Similar foci of α-catenin and Armadillo have been documented in the central wing pouch of *Drosophila* (Somorjai and Martinez-Arias, 2008), although our studies provide the first evidence that these foci colocalize with inactivated DC. β-Catenin has non-overlapping binding sites for Axin and α-catenin (Pokutta and Weis, 2000; Aberle et al., 1996; Behrens et al., 1998) but it remains to be determined whether such indirect recruitment occurs and is functionally significant for DC inactivation. Alternatively, the inactivating conformational change in the DC may allow APC proteins to bind α-catenin, which then serves as a high-affinity binding site for β-catenin (Choi et al., 2013), allowing for efficient accumulation of both proteins.

The architecture of wing disc cells, combined with pulsed Wnt signaling and the ability to observe DCs with BiFC, revealed foci of active DC in the cytoplasm of the cell body, as well as in apical and basal cellular regions (Figs 1E,I and 2A). Proximity to the nucleus suggests the surrounding cytoplasm is of particular importance for active DC in preventing nuclear signaling by β-catenin/Armadillo. The ligand-activated receptor transiently interacts with active DCs, inducing an inactivating conformational change, which subsequently assembles inactivated DCs into one or two large super-complexes per cell (Fig. 7, Fig. S4G-I). Although our analysis suggests that these super-complexes are an order of magnitude larger than active DCs (Fig. S4I), a detailed analysis of the precise size of DCs and super-complexes will require analysis by electron microscopy. Irrespective of the precise size of complexes, the model is consistent with the notion that active DCs are present throughout the cytoplasm but are inactivated and assembled into large complexes in response to Wnt signaling. A cytoplasm depleted of active DC then allows for accumulation of and nuclear signaling by β-catenin (Fig. 7).

Core pathway activity versus signal modulation

A prominent model postulates that 'signalosomes' are sites of DC inactivation, where large DC aggregates form and persist at ligand-activated receptors (Bilic et al., 2007; Taelman et al., 2010; Yamamoto et al., 2006; Hagemann et al., 2014). However, this model derives from studies that relied on overexpression of Axin, Dishevelled or both. Under such conditions, aggregates of these proteins form even in unstimulated cells, calling into question the physiological relevance of the reported protein-protein interactions (Bilic et al., 2007; Schwarz-Romond et al., 2005; Schwarz-Romond et al., 2007a; Pronobis et al., 2015). Pivotal to both aggregation and the signalosome model are DIX domains present in Axin and Dishevelled, as they drive the formation of super-complexes. In the signalosome model, interactions between the DIX domains of Axin and Dishevelled are proposed to inactivate the DC, while another proposed mechanism for DC inactivation invokes a phosphorylation-induced conformational change involving the DIX domain of Axin that prevents DC access to β-catenin (Kim et al., 2013). However, rescue experiments demonstrate that the C terminus of Axin (including the DIX domain) is largely dispensable both for DC activity and its inactivation *in vivo* (Peterson-Nedry et al., 2008), suggesting that the DIX domain does not play a crucial role in the core signaling pathway. Rather, signaling mechanisms involving the DIX domains of Axin and Dishevelled may represent accessory elements involved in context-dependent signal modulation.

We expect that long-range patterning by the Wnt signaling gradient depends on multiple modulatory mechanisms that cooperate to refine the signal generated by the core pathway. Several of these mechanisms, including localization, sequestration or intracellular transport of signaling components, may function in different contexts. The analysis of where and in what combination these mechanisms function will derive from the investigation of Wnt signaling *in vivo*, benefiting from the application of BiFC protocols.

MATERIALS AND METHODS

BiFC constructs

Axin was tagged N-terminally with Ven2 (Ven2-^{N}Axin) or internally after H427 (Axin^{M}-Ven2; Peterson-Nedry et al., 2008). Ven1 and Ven2 were a gift from S. Michnick, University of Montreal, QC, Canada (Benton et al., 2006). Ven1 was fused to the C terminus of Sgg containing an N-terminal 3xHA-tag (Sgg-Ven1). Similarly, Ven1 was fused to the C terminus of APC2 (APC2-Ven1). Fusion fragments were cloned into tub-promoter vectors with a white^{+} flip-out cassette inserted for inducible expression, generating plasmids for germ-line transformation (Peterson-Nedry et al., 2008). None of these constructs interfered with endogenous Wg signaling, and Venus fusion constructs were capable of rescuing null mutants of the target genes to the extent expected from previous analyses (Peterson-Nedry et al., 2008): rescue by Ven2-^{N}Axin, embryonic rescue by Axin^{M}-Ven2, rescue of *apc apc2* by Ven1-APC2 and APC2-Ven1 (Sgg-Ven1 is inactive due to a kinase mutation and does not interfere with development). BiFC signal was detected only following co-expression of specific combinations (Ven2-^{N}Axin+APC2-Ven1 and Axin^{M}-Ven2+Sgg-Ven1, but not with Ven2-^{N}Axin+Sgg-Ven1) (Fig. S2E-G), indicating stringent conformational and structural constraints that underlie the specificity of BiFC technology.

Drosophila genetics

Larval genotypes

y w was used as control strain. tub>w+>Ven2-^{N}Axin and tub>w+>APC2-Ven1 were generated by P-element mediated transformation. phiC31 integrase-mediated transformation was used to target tub>w+Axin^{M}Ven2 to PBac{y[+]-attP-3B}VK00002 at chromosomal location 28E7 and tub>w+>3xHA-Sgg-Ven1 to PBac{y[+]-attP-9A}VK00019 at chromosomal location 68D2. FlyBase lists *wg*^{ts} as *wg*$^{l-12}$ and *wg*^{CX3} as *wg*$^{l-16}$. tub>w+>Fz2-myc and tub>w+>Fz2-EGFP are from Baig-Lewis et al. (2007). The Sgg-GFP trap sgg^{ZCL1912} (BDSC #50887, a kind gift from L. Cooley, Yale University, New Haven, CT, USA) was used for larval extracts (Fig. S1A).

Genotypes used were as follows: Fig. 1A,B and Fig. S3B, *y w* hs>flp (FL122; ry+); wg>Gal4^{MD758}/CyO; UAS>mCD8-GFP/+; Fig. 1D and Fig. S2D, *y w* hs>flp (FL122; ry+); +/+; tub>HA-Sgg-Ven1; Figs 1H-I, 2A, S1A,C and S2H,M, *y w* hs>flp (FL122; ry+); [tub>Axin^{M}Ven2; tub>HA-Sgg-Ven1]/T(2;3) CyO-TM6B; Fig. 2A,C, *y w* hs>flp (FL122; ry+); tub>Axin^{M}Ven2/*ptc*>Gal4; tub>HA-Sgg-Ven1/UAS>Fz2-myc; Fig. 3A,B, *y w* hs>flp (FL122; ry+); *wg*^{ts}, tub>Axin^{M}Ven2/*wg*^{CX4}; tub>HA-Sgg-Ven1/+; Fig. 3C, *y w* hs>flp (FL122; ry+); *ptc*>Gal4; UAS>Wg^{WT}; Fig. 3D, E, *y w* hs>flp (FL122; ry+); *ptc*>Gal4; UAS>Wg^{ts}; Fig. 3F, *y w* hs>flp (FL122; ry+); ptc>Gal4, Gal80^{ts}, tub>Axin^{M}Ven2/tub>Axin^{M}Ven2; tub>HA-Sgg-Ven1, UAS>Wg^{ts}/tub>HA-Sgg-Ven1, tub>Fz2-myc; Figs 4A, 5A-D,F-H and S1D, *y w* hs>flp (FL122; ry+); tub>APC2-Ven1; tub>Ven2-^{N}Axin; Fig. 5E, *y w* hs>flp (FL122; ry+); tub>APC2-Ven1/ptc>Gal4; tub>Ven2-^{N}Axin/UAS>Fz2-myc; Fig. 4D,E and Fig. S5, *y w* hs>flp (FL122; ry+); *wg*^{ts}, tub>APC2-Ven1/*wg*^{CX4}; tub>Ven2-^{N}Axin/+; Fig. 4F, *y w* hs>flp (FL122; ry+); tub>APC2-Ven1/ptc>Gal4, G80^{ts}; tub>Ven2-^{N}Axin/UAS>NrtWg; Fig. 6A-C, *y w* hs>flp (FL122; ry+); tub>APC2-Ven1/

Development (2019) 146, dev164145. doi:10.1242/dev.164145

ptc>Gal4, G80^{ts}; tub>Ven2-^{N}Axin/UAS>Wg^{ts}; Fig. S2G, *y w* hs>flp (FL122; ry+); +/+; tub>Ven2-^{N}Axin/tub>HA-Sgg-Ven1; Figs S1B and S2I, *w*; tub>APC2V1; apc^{Q8} apc2^{g10}/apc^{Q8} apc2^{g10}; Fig. S3F, *y w* hs>flp (FL122; ry+); *ptc*>Gal4/+; UAS>Wg^{ts}/tub>Fz2-EGFP; Fig. 3A,B, *y w* hs>flp (FL122; ry+); *wg*^{ts}, tub>Axin^{M}Ven2/*wg*^{CX4}; tub>HA-Sgg-Ven1/+ or *y w* Ubx>flp; *wg*^{ts}, tub>Axin^{M}Ven2/*wg*^{CX3}; tub>HA-Sgg-Ven1/+; and Figs. S4, *y w* hs>flp (FL122; ry+); tub>w+>APC2-Ven1/UAS>flp; tub>w+>Ven2-Axin/Hh>Gal4, Gal80^{ts}.

Control of expression

BiFC constructs were activated by removing the white+ cassette (Peterson-Nedry et al., 2008). The Gal4/UAS system was used for *ptc*>Gal4 driven expression of Wg and Wg^{ts} (Fig. S3; Brand and Perrimon, 1993; Hays et al., 1997; Wilder and Perrimon, 1995). Temperature-sensitive Gal80^{ts} repressed Gal4 at ≤25°C until its inactivation at 30°C, thereby averting lethality associated with ectopic Wg expression. Pulsed Wg^{ts} signal was generated in third instar larvae carrying *ptc*>Gal4 Gal80^{ts} and UAS-Wg^{ts}, by loading cells in the *ptc* stripe with Wg^{ts} protein that is secretion deficient at 30°C (Fig. S3). A shift to 16°C allowed the timing of the release of Wg^{ts}. Temperature shifts for timed incubations were performed by moving larvae to vials with food equilibrated to the target temperature.

For timed inactivation of Wg signaling, Axin^{M}-Sgg BiFC constructs were induced through heat-shock of brown pupae; resulting males were mated to virgins of [*wg*^{ts}; +]/T(2;3)CyO-TMB (or [*wg*^{1}; +]/T(2;3)CyO-TM6B; below). Flies carrying the *wg*^{ts} and *wg*^{CX4} alleles were reared at 16°C and shifted to 30°C. Non-balancer larvae were identified as Tb+, using the balancer T(2;3) CyO-TM6B. Viability was low for wg^{ts}/wg^{CX4} Axin^{M}-Sgg animals although three wing discs were obtained for each of both experiment and control conditions (Fig. 3A,B). For better survival of animals and to confirm results, signaling was also inactivated in *wg*^{ts}/*wg*^{CX3} animals (Couso et al., 1993). Fisher's exact tests were used to determine statistical significance.

The timing of signaling events may be standardized to 25°C for experiments performed at different temperature to facilitate comparisons. As the rate of biological processes is temperature dependent, incubation times obtained at 16°C may be multiplied by 0.5 while incubation times obtained at 30°C may be multiplied by 1.2 to obtain the approximate duration for the biological process at 25°C. This approximation assumes that the length of the life cycle scales linearly with temperature throughout development, including the process of Wg signal transduction (~440 h at 16°C, ~220 h at 25°C and ~190 h at 30°C; Roberts, 1998). Currently, this has only been determined for prolonged periods during *Drosophila* development (Kuntz and Eisen, 2014).

Immunohistochemistry and cryosectioning

Third instar wing disc dissections and staining were performed as described (Klein, 2008), except that primary antibodies were incubated overnight at 4°C and anti-Arl8 was incubated in PBS/5% normal donkey serum/0.02% saponin (instead of 0.1% Triton X-100). For cryosectioning, stained wing discs were post-fixed for 30 min at room temperature in PBT/4% formaldehyde to immobilize antibodies, washed and embedded in 10% gelatin/30% sucrose/PBS. Sections of 10-25 µm were cut on a Leica CM1850 cryostat and mounted on slides with Fluoromount-G (SouthernBiotech). For a detailed description of embedding and cryosectioning protocols, see Petshow and Wehrli (2018).

Primary antibodies used in this study were: rat anti-APC2 (a gift from M. Peifer, University of North Carolina, Chapel Hill, NC, USA; 1:1000; McCartney et al., 1999), rat anti-α-catenin (DSHB, DCAT-1, concentrate 1:200), rat anti-E-Cadherin (DSHB, DCAD2, concentrate 1:100), mouse anti-Arm (DSHB, N2 7A1, concentrate 1:800), mouse anti-Wg (DSHB, 4D4, concentrate 1:600), rabbit anti-Arl8 (a gift from S. Munro, MRC-Laboratory of Molecular Biology, Cambridge, UK; 1:2000; Rosa-Ferreira and Munro, 2011), mouse anti-Dll (a gift from Dianne Duncan, Washington University, St. Louis, MO, USA; 1:300; Diaz-Benjumea and Cohen, 1995; Duncan et al., 1998), chicken anti-GFP (Aves Labs, GFP1020 #1223FP03, 1:1000), rabbit anti-GFP (Abcam, ab6556 #GR76756-1, 1:600), rat anti-HA (Roche, 3F10 #11447800, 1:2000), guinea pig anti-Sens (a gift from H. Bellen, Baylor College of Medicine, Houston, TX, USA, 1:1000; Jafar-Nejad et al., 2003), rabbit anti-myc (Abcam, ab9601 GR20094, 1:2000) and mouse anti-γ-tubulin (Sigma, GTU-88 096H4821, 1:10,000). Monoclonal antibodies that specifically detect the assembled Ven1/Ven2 complex were used to enhance the detection of weak BiFC signals: GFP-20 (Sigma G-6539 112M4763, 1:2000; Gordon and Scott, 2009), clone 3E6 (Invitrogen, A11120 1563696; 1:750, this study) and rabbit monoclonal anti-GFP (ThermoFisher, G10362 1787904; 1:1200; this study). Ven1 and Ven2 fragments were detected by goat anti-GFP (Novus Biologicals, NB100-1770 33301; 1:1000; this study). Hoechst 33258 was used to label nuclear DNA. Fluorescently labeled secondary antibodies were from Invitrogen (anti-rabbit A647, A21244 1463166, 1:1000; anti-rat A568, A11077 1512105, 1:750; anti-goat A568, A11057 93E1-1; 1:1000) and Jackson ImmunoResearch (anti-rat A488, 712-545-153 128270, 1:800; anti-ratA647, 712-605-153 127806 and 115022, 1:400; anti-rabbit DyLight488, 711-485-152 83832, 1:200; anti-rabbit DyLight, 711-505-152 80373, 1:200; anti-guinea pig A647, 706-605-148 #113411, 1:200; anti-chicken DyLightA488, 703-485-155 84338, 1:200; and anti-chicken DyLightA549, 103-505-155 81207, 1:200). Anti-mouse IgG subtype-specific secondary antibodies were: anti-IgG1A488, 115-545-205 112835, 1:300; anti-Ig1RRX, 115-295-205 #113818, 1:300; anti-IgG1A647, 115-605-205 113613; anti-IgG2aA488, 115-545-206 109994, 1:300; anti-IgG2aRRX, 115-295-206 109994, 1:300; anti-IgG2aA647, 115-605-206 128604, 1:400; anti-IgG2bA488, 115-545-207 120903, 1:300; and anti-IgG2bA647, 115-605-207 119989, 1:200 (Jackson ImmunoResearch). Double labeling to differentiate between different isotypes of mouse monoclonal antibodies was achieved by using IgG subtype-specific secondary antibodies (Jackson ImmunoResearch; Manning et al., 2012). Of these, anti-IgG1A488 (115-545-205 112835) and anti-Ig1RRX (115-295-205 113818) cross-reacted with rat antibodies but anti-IgG1A647 (115-605-205 113613) did not. Cross-reactivity was avoided by sequential staining. For example, anti-IgG1RRX incubation was followed by washes and fixation (15 min on ice) before incubations with rat primary and anti-rat secondary antibodies were performed. Specificity of antibodies was confirmed using differently labeled secondary antibodies, staining of tissue without epitope (if applicable) or locally limited induction of construct expression. For example, antibodies recognizing Ven1 and Ven2 were identified by staining tissue after local induction of Ven1 and Ven2 constructs (using *ptc*>GAL4×UAS>flipase; Fig. S8).

Quantification of construct expression by immunoblotting

Larval lysates were prepares as described by Wang et al. (2016b). Briefly, third instar larvae were dissected in ice-cold PBS; salivary glands, gut and fat body were removed. PBS was removed and 8 µl reducing sample buffer added for each larval carcass. Samples were vortexed, incubated for 5 min at 95°C, 5 min on ice, centrifuged, the supernatant transferred and loaded onto Criterion gels (BioRad). Criterion 4-12% BisTris/MOPS gels were used to separate the Sgg and APC2 proteins. Immunofluorescence was successful for Sgg but APC2 detection required the increased sensitivity provided by chemiluminescence.

Axin antisera detected background bands, where some co-migrated with constructs on Criterion 4-12% BisTris/MOPS gels and Criterion 3-8% Tris-Acetate gels. The separation was improved on Criterion 7.5% TGX gels. Immunopositive bands were detected using Azure c600 (Azure Biosystems) and quantified using automated band detection in AzureSpot. Automated background subtraction was applied. Ven2-Axin and FLAG-AxinVen2 constructs co-migrated with background bands. The relative abundance of these background bands to stronger background bands was determined using reference samples. This relationship was then used in background subtraction in order to reveal the amount of Axin present. Excel was used to calculate mean and standard deviation values.

Antibodies for immmunoblotting

Anti-Sgg 4G-1E monoclonal was used at 1:1000 (EMD Millipore, 05-412, 3104249; identical to 4G1E11, Papadopoulou et al., 2004) and detected using goat anti-mouse A680 at 1:1000 (Invitrogen, A21058 84C2-1). Guinea pig anti-APC2 (GP10, 1:5000, Takacs et al., 2008) and guinea pig anti-Axin (GP91, 1:1000, Wang et al., 2016b) antisera were kindly provided by Y. Ahmed, Dartmouth Geisel School of Medicine, Hanover, NH, USA. They were detected using donkey anti-guinea pig HRP conjugate (1:10000, Jackson ImmunoResearch 706-035-148) and Supersignal West Pico Plus Chemiluminescent Substrate (Thermo Scientific, 34580, TH271013).

Development (2019) 146, dev164145. doi:10.1242/dev.164145

Sample size, replication and controls

At least six wing discs were analyzed for each condition (except where noted) and findings confirmed in replicated experiments. BiFC signal versus background was determined using restricted expression of constructs (Fig. S4A-D; *hh*>Gal4, G80^{ts}, UAS>flp; *ptc*>Gal4, G80^{ts} UAS>flp; and not shown). This approach was also used to verify the specificity of anti-GFP and of secondary antibodies (Fig. S8). Surprisingly, we detected strong cross-reactivity with *Drosophila* tissue using several commercially available secondary antibodies, as well as two ascite preparations of primary antibodies, suggesting exposure of host animals to stinging insects. To reduce potential background and increase specificity in the detection of weak signals, antibodies were pre-adsorbed using fixed *Drosophila* embryos.

Profiles of signal distributions across the curved epithelium of the wing pouch

Confocal images were imported into ImageJ64, which was used to quantify fluorescent intensities across the wing pouch. Using the inner and outer boundary of the epithelium, an algorithm was used to divide the epithelium into a predefined number of polygons (n=100; resembling columnar cells, Fig. S2B-D; the source code of the ImageJ plug-in has been deposited in GitHub, see https://github.com/petshows/Imaginal-Disc-Profile). The sum of pixel intensities was quantified and standardized to the area in each polygon, then exported to Excel. For z-stacks, each section was quantified separately, values exported to Excel, summed and averaged (typically three to six discs). For comparison, maximal values were standardized to a value of 1, representing arbitrary units (a.u.).

Collection fluorescent images and assessment of signal colocalization

Samples were imaged on a Zeiss LSM 780 or Zeiss Elyra PS.1 with Airyscan detection. Comparable settings were used to image all preparations in an experiment (e.g. images in Fig. 3A,B were collected with identical settings), except that the laser intensity for the BiFC detection in 2B had to be reduced from 30% to 15% to obtain intensities within the linear range of the detector.

Image analysis

Imaris (versions 8.4.2 and 9.0) was used to visualize and quantify fluorescent objects using spot detection and object-based approaches, as well as to determine signal intensity. Imaris was used on original images to determine Pearson's Correlation Coefficient (PCC) and thresholded Manders' Correlation Coefficient (MCC), which uses an algorithm for automatic threshold detection (Costes et al., 2004). Additional verification for CCs may be obtained if a shift of one channel relative to the other significantly reduces CC values. We shifted one channel by the diameter of the largest object (typically ∼0.30 µm). Values are listed in Table 1.

Counting BiFC objects and determination of their apparent size

Airyscan super-resolution image stacks (.czi format) were imported into Imaris and background subtracted (median filter, threshold cutoff). The algorithm of the 'spot' function was then used to identify BiFC objects. We noticed that margin effects of the median filter function generated a large number of artefactual spots in the outermost five pixels (0.35 µm) of the z-stack volume, which we eliminated from analysis. The number of spots present in a volume of interest, identified using the 'surface' function, was then determined. To measure the apparent size of BiFC objects, the surface function was used to represent them as objects. Objects contained only partly within the z-stack were excluded from the analysis, as they represent partial BiFC objects. Imaris was also used to create videos and screen shots. Figures were assembled using Adobe Photoshop CS3 and PowerPoint.

Acknowledgements

We are grateful for comments and improvement to the manuscript from Drs P. F. Copenhaver, P. Barr-Gillespie, I. Carrin, C. Enns, T. Howard, P. A. Lawrence, P. Streeter, G. Struhl, A. Tomlinson, E. Verheyen and M. H. Wong, as well as for discussion and advice from Drs S. Kaech, M. Peifer, A. Nechiporuk, S. Speese, A. Snyder, A.-S. Zhang, Y. Ahmed and M. Deza-Culbertson. We acknowledge the Developmental Studies Hybridoma Bank and the Bloomington *Drosophila* Stock Center.

Competing interests

The authors declare no competing or financial interests.

Author contributions

Conceptualization: D.B.L., M.N., J.M.L., M.B., S.P., K.H., M.W.; Methodology: D.B.L., M.N., J.M.L., M.B., S.P., K.H., M.W.; Software: S.P., G.S.; Validation: D.B.L., M.N., J.M.L., M.B., S.P., K.H., M.W.; Investigation: D.B.L., M.N., J.M.L., M.B., S.P., K.H., M.W.; Resources: M.W.; Writing - original draft: D.B.L., M.N., M.W.; Writing - review & editing: D.L., M.B., S.P., K.H., G.S., M.W.; Visualization: G.S., M.W.; Supervision: M.W.; Project administration: M.W.; Funding acquisition: M.W.

Funding

This work was supported by grants from the National Institutes of Health (R01GM67029 and R01GM103876), the National Science Foundation (IOS-1021573 and IOS-1353799), and the Oregon Health and Science University Medical Research Foundation to M.W. Deposited in PMC for release after 12 months.

Supplementary information

Supplementary information available online at
http://dev.biologists.org/lookup/doi/10.1242/dev.164145.supplemental

References

Aberle, H., Schwartz, H., Hoschuetzky, H. and Kemler, R. (1996). Single amino acid substitutions in proteins of the armadillo gene family abolish their binding to alpha-catenin. *J. Biol. Chem.* **271**, 1520-1526. doi:10.1074/jbc.271.3.1520

Adler, J. and Parmryd, I. (2010). Quantifying colocalization by correlation: the Pearson correlation coefficient is superior to the Mander's overlap coefficient. *Cytometry A* **77A**, 733-742. doi:10.1002/cyto.a.20896

Baig-Lewis, S., Peterson-Nedry, W. and Wehrli, M. (2007). Wingless/Wnt signal transduction requires distinct initiation and amplification steps that both depend on Arrow/LRP. *Dev. Biol.* **306**, 94-111. doi:10.1016/j.ydbio.2007.03.005

Behrens, J., Jerchow, B. A., Wurtele, M., Grimm, J., Asbrand, C., Wirtz, R., Kuhl, M., Wedlich, D. and Birchmeier, W. (1998). Functional interaction of an axin homolog, conductin, with beta-catenin, Apc, and GSK3beta. *Science* **280**, 596-599. doi:10.1126/science.280.5363.596

Benton, R., Sachse, S., Michnick, S. W. and Vosshall, L. B. (2006). Atypical membrane topology and heteromeric function of Drosophila odorant receptors in vivo. *PLoS Biol.* **4**, e20. doi:10.1371/journal.pbio.0040020

Bilic, J., Huang, Y.-L., Davidson, G., Zimmermann, T., Cruciat, C.-M., Bienz, M. and Niehrs, C. (2007). Wnt induces LRP6 signalosomes and promotes dishevelled-dependent LRP6 phosphorylation. *Science* **316**, 1619-1622. doi:10.1126/science.1137065

Brand, A. H. and Perrimon, N. (1993). Targeted gene expression as a means of altering cell fates and generating dominant phenotypes. *Development* **118**, 401-415.

Choi, S. H., Estaras, C., Moresco, J. J., Yates, J. R., III and Jones, K. A. (2013). alpha-Catenin interacts with APC to regulate beta-catenin proteolysis and transcriptional repression of Wnt target genes. *Genes Dev.* **27**, 2473-2488. doi:10.1101/gad.229062.113

Clevers, H. and Nusse, R. (2012). Wnt/beta-catenin signaling and disease. *Cell* **149**, 1192-1205. doi:10.1016/j.cell.2012.05.012

Cliffe, A., Hamada, F. and Bienz, M. (2003). A role of Dishevelled in relocating Axin to the plasma membrane during wingless signaling. *Curr. Biol.* **13**, 960-966. doi:10.1016/S0960-9822(03)00370-1

Costes, S. V., Daelemans, D., Cho, E. H., Dobbin, Z., Pavlakis, G. and Lockett, S. (2004). Automatic and quantitative measurement of protein-protein colocalization in live cells. *Biophys. J.* **86**, 3993-4003. doi:10.1529/biophysj.103.038422

Couso, J. P., Bate, M. and Martinez-Arias, A. (1993). A wingless-dependent polar coordinate system in Drosophila imaginal discs. *Science* **259**, 484-489. doi:10.1126/science.8424170

Couso, J. P., Bishop, S. A. and Martinez Arias, A. (1994). The wingless signalling pathway and the patterning of the wing margin in *Drosophila*. *Development* **120**, 621-636.

Davidson, G., Wu, W., Shen, J., Bilic, J., Fenger, U., Stannek, P., Glinka, A. and Niehrs, C. (2005). Casein kinase 1 gamma couples Wnt receptor activation to cytoplasmic signal transduction. *Nature* **438**, 867-872. doi:10.1038/nature04170

Diaz-Benjumea, F. J. and Cohen, S. M. (1995). Serrate signals through Notch to establish a Wingless-dependent organizer at the dorsal/ventral compartment boundary of the Drosophila wing. *Development* **121**, 4215-4225.

Duncan, D. M., Burgess, E. A. and Duncan, I. (1998). Control of distal antennal identity and tarsal development in Drosophila by spineless-aristapedia, a homolog of the mammalian dioxin receptor. *Genes Dev.* **12**, 1290-1303. doi:10.1101/gad.12.9.1290

Dunn, K. W., Kamocka, M. M. and Mcdonald, J. H. (2011). A practical guide to evaluating colocalization in biological microscopy. *Am. J. Physiol. Cell Physiol.* **300**, C723-C742. doi:10.1152/ajpcell.00462.2010

Gerlach, J. P., Emmink, B. L., Nojima, H., Kranenburg, O. and Maurice, M. M. (2014). Wnt signalling induces accumulation of phosphorylated beta-catenin in two distinct cytosolic complexes. *Open Biol.* **4**, 140120. doi:10.1098/rsob.140120

González, F., Swales, L., Bejsovec, A., Skaer, H. and Martinez Arias, A. (1991). Secretion and movement of *wingless* protein in the epidermis of the *Drosophila* embryo. *Mech. Dev.* **35**, 43-54. doi:10.1016/0925-4773(91)90040-D

Gordon, M. D. and Scott, K. (2009). Motor control in a Drosophila taste circuit. *Neuron* **61**, 373-384. doi:10.1016/j.neuron.2008.12.033

Habib, S. J., Chen, B.-C., Tsai, F.-C., Anastassiadis, K., Meyer, T., Betzig, E. and Nusse, R. (2013). A localized Wnt signal orients asymmetric stem cell division in vitro. *Science* **339**, 1445-1448. doi:10.1126/science.1231077

Hagemann, A. I. H., Kurz, J., Kauffeld, S., Chen, Q., Reeves, P. M., Weber, S., Schindler, S., Davidson, G., Kirchhausen, T. and Scholpp, S. (2014). In vivo analysis of formation and endocytosis of the Wnt/beta-catenin signaling complex in zebrafish embryos. *J. Cell Sci.* **127**, 3970-3982. doi:10.1242/jcs.148767

Hays, R., Gibori, G. B. and Bejsovec, A. (1997). Wingless signaling generates pattern through two distinct mechanisms. *Development* **124**, 3727-3736.

Hedgepeth, C. M., Deardorff, M. A., Rankin, K. and Klein, P. S. (1999). Regulation of glycogen synthase kinase 3beta and downstream Wnt signaling by axin. *Mol. Cell. Biol.* **19**, 7147-7157. doi:10.1128/MCB.19.10.7147

Huang, S.-M. A., Mishina, Y. M., Liu, S., Cheung, A., Stegmeier, F., Michaud, G. A., Charlat, O., Wiellette, E., Zhang, Y., Wiessner, S. et al. (2009). Tankyrase inhibition stabilizes axin and antagonizes Wnt signalling. *Nature* **461**, 614-620. doi:10.1038/nature08356

Ikeda, S., Kishida, S., Yamamoto, H., Murai, H., Koyama, S. and Kikuchi, A. (1998). Axin, a negative regulator of the Wnt signaling pathway, forms a complex with GSK-3beta and beta-catenin and promotes GSK-3beta-dependent phosphorylation of beta-catenin. *EMBO J.* **17**, 1371-1384. doi:10.1093/emboj/17.5.1371

Itoh, K., Brott, B. K., Bae, G.-U., Ratcliffe, M. J. and Sokol, S. Y. (2005). Nuclear localization is required for Dishevelled function in Wnt/beta-catenin signaling. *J. Biol.* **4**, 3. doi:10.1186/jbiol20

Jafar-Nejad, H., Acar, M., Nolo, R., Lacin, H., Pan, H., Parkhurst, S. M. and Bellen, H. J. (2003). Senseless acts as a binary switch during sensory organ precursor selection. *Genes Dev.* **17**, 2966-2978. doi:10.1101/gad.1122403

Jafar-Nejad, H., Tien, A. C., Acar, M. and Bellen, H. J. (2006). Senseless and Daughterless confer neuronal identity to epithelial cells in the Drosophila wing margin. *Development* **133**, 1683-1692. doi:10.1242/dev.02338

Kim, S.-E., Huang, H., Zhao, M., Zhang, X., Zhang, A., Semonov, M. V., Macdonald, B. T., Zhang, X., Garcia Abreu, J., Peng, L. et al. (2013). Wnt stabilization of beta-catenin reveals principles for morphogen receptor-scaffold assemblies. *Science* **340**, 867-870. doi:10.1126/science.1232389

Klein, T. (2008). Immunolabeling of imaginal discs. In *Drosophila: Methods and Protocols* (ed. C. Dahmann), pp. 253-263. Totowa, NJ: Humana Press.

Kuntz, S. G. and Eisen, M. B. (2014). Drosophila embryogenesis scales uniformly across temperature in developmentally diverse species. *PLoS Genet.* **10**, e1004293. doi:10.1371/journal.pgen.1004293

Lee, E., Salic, A., Krüger, R., Heinrich, R. and Kirschner, M. W. (2003). The roles of APC and Axin derived from experimental and theoretical analysis of the Wnt pathway. *PLoS Biol.* **1**, e10. doi:10.1371/journal.pbio.0000010

Li, V. S. W., Ng, S. S., Boersema, P. J., Low, T. Y., Karthaus, W. R., Gerlach, J. P., Mohammed, S., Heck, A. J. R., Maurice, M. M., Mahmoudi, T. et al. (2012). Wnt signaling through inhibition of beta-catenin degradation in an intact Axin1 complex. *Cell* **149**, 1245-1256. doi:10.1016/j.cell.2012.05.002

Liu, T., Liu, X., Wang, H., Moon, R. T. and Malbon, C. C. (1999). Activation of rat frizzled-1 promotes Wnt signaling and differentiation of mouse F9 teratocarcinoma cells via pathways that require Galpha(q) and Galpha(o) function. *J. Biol. Chem.* **274**, 33539-33544. doi:10.1074/jbc.274.47.33539

Manning, C. F., Bundros, A. M. and Trimmer, J. S. (2012). Benefits and pitfalls of secondary antibodies: why choosing the right secondary is of primary importance. *PLoS ONE* **7**, e38313. doi:10.1371/journal.pone.0038313

Mao, J., Wang, J., Liu, B., Pan, W., Farr, G. H., III, Flynn, C., Yuan, H., Takada, S., Kimelman, D., Li, L. and et al. (2001). Low-density lipoprotein receptor-related protein-5 binds to Axin and regulates the canonical Wnt signaling pathway. *Mol. Cell* **7**, 801-809. doi:10.1016/S1097-2765(01)00224-6

Mao, B., Wu, W., Davidson, G., Marhold, J., Li, M., Mechler, B. M., Delius, H., Hoppe, D., Stannek, P., Walter, C. et al. (2002). Kremen proteins are Dickkopf receptors that regulate Wnt/beta-catenin signalling. *Nature* **417**, 664-667. doi:10.1038/nature756

McCartney, B. M. and Peifer, M. (2003). Stem cells in the news: CNN and APC make headlines. *Dev. Cell* **5**, 532-534. doi:10.1016/S1534-5807(03)00300-9

McCartney, B. M., Dierick, H. A., Kirkpatrick, C., Moline, M. M., Baas, A., Peifer, M. and Bejsovec, A. (1999). Drosophila APC2 is a cytoskeletally-associated protein that regulates wingless signaling in the embryonic epidermis. *J. Cell Biol.* **146**, 1303-1318. doi:10.1083/jcb.146.6.1303

Mcdonald, J. H. and Dunn, K. W. (2013). Statistical tests for measures of colocalization in biological microscopy. *J. Microsc.* **252**, 295-302. doi:10.1111/jmi.12093

Michnick, S. W., Ear, P. H., Manderson, E. N., Remy, I. and Stefan, E. (2007). Universal strategies in research and drug discovery based on protein-fragment complementation assays. *Nat. Rev. Drug Discov.* **6**, 569-582. doi:10.1038/nrd2311

Neumann, C. J. and Cohen, S. M. (1997). Long-range action of Wingless organizes the dorsal-ventral axis of the Drosophila wing. *Development* **124**, 871-880.

Papadopoulou, D., Bianchi, M. W. and Bourouis, M. (2004). Functional studies of shaggy/glycogen synthase kinase 3 phosphorylation sites in Drosophila melanogaster. *Mol. Cell. Biol.* **24**, 4909-4919. doi:10.1128/MCB.24.11.4909-4919.2004

Park, J.-I., Ji, H., Jun, S., Gu, D., Hikasa, H., Li, L., Sokol, S. Y. and Mccrea, P. D. (2006). Frodo links Dishevelled to the p120-catenin/Kaiso pathway: distinct catenin subfamilies promote Wnt signals. *Dev. Cell* **11**, 683-695. doi:10.1016/j.devcel.2006.09.022

Peterson-Nedry, W., Erdeniz, N., Kremer, S., Yu, J., Baig-Lewis, S. and Wehrli, M. (2008). Unexpectedly robust assembly of the Axin destruction complex regulates Wnt/Wg signaling in Drosophila as revealed by analysis in vivo. *Dev. Biol.* **320**, 226-241. doi:10.1016/j.ydbio.2008.05.521

Petshow, S. and Wehrli, M. (2018). Preparation of precisely oriented cryosections of undistorted drosophila wing imaginal discs for high resolution confocal imaging. *Bio. Protoc.* **8**, e2725. doi:10.21769/BioProtoc.2725

Piao, S., Lee, S.-H., Kim, H., Yum, S., Stamos, J. L., Xu, Y., Lee, S.-J., Lee, J., Oh, S., Han, J.-K. et al. (2008). Direct inhibition of GSK3beta by the phosphorylated cytoplasmic domain of LRP6 in Wnt/beta-catenin signaling. *PLoS ONE* **3**, e4046. doi:10.1371/journal.pone.0004046

Pokutta, S. and Weis, W. I. (2000). Structure of the dimerization and beta-catenin-binding region of alpha-catenin. *Mol. Cell* **5**, 533-543. doi:10.1016/S1097-2765(00)80447-5

Pronobis, M. I., Rusan, N. M. and Peifer, M. (2015). A novel GSK3-regulated APC: Axin interaction regulates Wnt signaling by driving a catalytic cycle of efficient betacatenin destruction. *eLife* **4**, e08022. doi:10.7554/eLife.08022

Pulipparacharuvil, S., Akbar, M. A., Ray, S., Sevrioukov, E. A., Haberman, A. S., Rohrer, J. and Kramer, H. (2005). Drosophila Vps16A is required for trafficking to lysosomes and biogenesis of pigment granules. *J. Cell Sci.* **118**, 3663-3673. doi:10.1242/jcs.02502

Roberts, D. B. (1998). *Drosophila: A Practical Approach*. Oxford, England; New York, IRL Press at Oxford University Press.

Roberts, D. M., Pronobis, M. I., Poulton, J. S., Waldmann, J. D., Stephenson, E. M., Hanna, S. and Peifer, M. (2011). Deconstructing the βcatenin destruction complex: mechanistic roles for the tumor suppressor APC in regulating Wnt signaling. *Mol. Biol. Cell* **22**, 1845-1863. doi:10.1091/mbc.e10-11-0871

Robida, A. M. and Kerppola, T. K. (2009). Bimolecular fluorescence complementation analysis of inducible protein interactions: effects of factors affecting protein folding on fluorescent protein fragment association. *J. Mol. Biol.* **394**, 391-409. doi:10.1016/j.jmb.2009.08.069

Rosa-Ferreira, C. and Munro, S. (2011). Arl8 and SKIP act together to link lysosomes to kinesin-1. *Dev. Cell* **21**, 1171-1178. doi:10.1016/j.devcel.2011.10.007

Rosin-Arbesfeld, R., Townsley, F. and Bienz, M. (2000). The APC tumour suppressor has a nuclear export function. *Nature* **406**, 1009-1012. doi:10.1038/35023016

Schaefer, K. N. and Peifer, M. (2019). Wnt/Beta-catenin signaling regulation and a role for biomolecular condensates. *Dev. Cell* **48**, 429-444. doi:10.1016/j.devcel.2019.01.025

Schaefer, K. N., Bonello, T. T., Zhang, S., Williams, C. E., Roberts, D. M., Mckay, D. J. and Peifer, M. (2018). Supramolecular assembly of the beta-catenin destruction complex and the effect of Wnt signaling on its localization, molecular size, and activity in vivo. *PLoS Genet.* **14**, e1007339. doi:10.1371/journal.pgen.1007339

Schwarz-Romond, T., Merrifield, C., Nichols, B. J. and Bienz, M. (2005). The Wnt signalling effector Dishevelled forms dynamic protein assemblies rather than stable associations with cytoplasmic vesicles. *J. Cell Sci.* **118**, 5269-5277. doi:10.1242/jcs.02646

Schwarz-Romond, T., Fiedler, M., Shibata, N., Butler, P. J. G., Kikuchi, A., Higuchi, Y. and Bienz, M. (2007a). The DIX domain of Dishevelled confers Wnt signaling by dynamic polymerization. *Nat. Struct. Mol. Biol.* **14**, 484-492. doi:10.1038/nsmb1247

Schwarz-Romond, T., Metcalfe, C. and Bienz, M. (2007b). Dynamic recruitment of axin by Dishevelled protein assemblies. *J. Cell Sci.* **120**, 2402-2412. doi:10.1242/jcs.002956

Somorjai, I. M. L. and Martinez-Arias, A. (2008). Wingless signalling alters the levels, subcellular distribution and dynamics of Armadillo and E-cadherin in third instar larval wing imaginal discs. *PLoS ONE* **3**, e2893. doi:10.1371/journal.pone.0002893

Spink, K. E., Polakis, P. and Weis, W. I. (2000). Structural basis of the Axin-adenomatous polyposis coli interaction. *EMBO J.* **19**, 2270-2279. doi:10.1093/emboj/19.10.2270

Struhl, G. and Basler, K. (1993). Organizing activity of wingless protein in Drosophila. *Cell* **72**, 527-540. doi:10.1016/0092-8674(93)90072-X

Sugioka, K., Mizumoto, K. and Sawa, H. (2011). Wnt regulates spindle asymmetry to generate asymmetric nuclear beta-catenin in C. elegans. *Cell* **146**, 942-954. doi:10.1016/j.cell.2011.07.043

Swarup, S. and Verheyen, E. M. (2012). Wnt/Wingless signaling in Drosophila. *Cold Spring Harb. Perspect. Biol.* **4**, a007930. doi:10.1101/cshperspect.a007930

Taelman, V. F., Dobrowolski, R., Plouhinec, J.-L., Fuentealba, L. C., Vorwald, P. P., Gumper, I., Sabatini, D. D. and de Robertis, E. M. (2010). Wnt signaling requires sequestration of glycogen synthase kinase 3 inside multivesicular endosomes. *Cell* **143**, 1136-1148. doi:10.1016/j.cell.2010.11.034

Takacs, C. M., Baird, J. R., Hughes, E. G., Kent, S. S., Benchabane, H., Paik, R. and Ahmed, Y. (2008). Dual positive and negative regulation of wingless signaling by adenomatous polyposis coli. *Science* **319**, 333-336. doi:10.1126/science.1151232

Tamai, K., Zeng, X., Liu, C., Zhang, X., Harada, Y., Chang, Z. and He, X. (2004). A mechanism for Wnt coreceptor activation. *Mol. Cell* **13**, 149-156. doi:10.1016/S1097-2765(03)00484-2

Tolwinski, N. S. (2009). Membrane bound axin is sufficient for Wingless signaling in Drosophila embryos. *Genetics* **181**, 1169-1173. doi:10.1534/genetics.108.098236

Tolwinski, N. S. and Wieschaus, E. (2001). Armadillo nuclear import is regulated by cytoplasmic anchor Axin and nuclear anchor dTCF/Pan. *Development* **128**, 2107-2117.

Tolwinski, N. S., Wehrli, M., Rives, A., Erdeniz, N., Dinardo, S. and Wieschaus, E. (2003). Wg/Wnt signal can be transmitted through arrow/LRP5,6 and Axin independently of Zw3/Gsk3beta activity. *Dev. Cell* **4**, 407-418. doi:10.1016/S1534-5807(03)00063-7

Valvezan, A. J., Zhang, F., Diehl, J. A. and Klein, P. S. (2012). Adenomatous polyposis coli (APC) regulates multiple signaling pathways by enhancing glycogen synthase kinase-3 (GSK-3) activity. *J. Biol. Chem.* **287**, 3823-3832. doi:10.1074/jbc.M111.323337

Van Den Heuvel, M., Harryman-Samos, C., Klingensmith, J., Perrimon, N. and Nusse, R. (1993). Mutations in the segment polarity genes wingless and porcupine impair secretion of the wingless protein. *EMBO J.* **12**, 5293-5302. doi:10.1002/j.1460-2075.1993.tb06225.x

Wang, Z., Tacchelly-Benites, O., Yang, E. and Ahmed, Y. (2016a). Dual roles for membrane association of Drosophila axin in Wnt signaling. *PLoS Genet.* **12**, e1006494. doi:10.1371/journal.pgen.1006494

Wang, Z., Tian, A., Benchabane, H., Tacchelly-Benites, O., Yang, E., Nojima, H. and Ahmed, Y. (2016b). The ADP-ribose polymerase Tankyrase regulates adult intestinal stem cell proliferation during homeostasis in Drosophila. *Development* **143**, 1710-1720. doi:10.1242/dev.127647

Wilder, E. L. and Perrimon, N. (1995). Dual functions of wingless in the Drosophila leg imaginal disc. *Development* **121**, 477-488.

Yamamoto, H., Komekado, H. and Kikuchi, A. (2006). Caveolin is necessary for Wnt-3a-dependent internalization of LRP6 and accumulation of beta-catenin. *Dev. Cell* **11**, 213-223. doi:10.1016/j.devcel.2006.07.003

Yang, E., Tacchelly-Benites, O., Wang, Z., Randall, M. P., Tian, A., Benchabane, H., Freemantle, S., Pikielny, C., Tolwinski, N. S., Lee, E. et al. (2016). Wnt pathway activation by ADP-ribosylation. *Nat. Commun.* **7**, 11430. doi:10.1038/ncomms11430

Zecca, M., Basler, K. and Struhl, G. (1996). Direct and long-range action of a wingless morphogen gradient. *Cell* **87**, 833-844. doi:10.1016/S0092-8674(00)81991-1

Zeng, X., Huang, H., Tamai, K., Zhang, X., Harada, Y., Yokota, C., Almeida, K., Wang, J., Doble, B., Woodgett, J. et al. (2008). Initiation of Wnt signaling: control of Wnt coreceptor Lrp6 phosphorylation/activation via frizzled, dishevelled and axin functions. *Development* **135**, 367-375. doi:10.1242/dev.013540

Zhang, L., Jia, J., Wang, B., Amanai, K., Wharton, K. A., Jr. and Jiang, J. (2006). Regulation of wingless signaling by the CKI family in Drosophila limb development. *Dev. Biol.* **299**, 221-237. doi:10.1016/j.ydbio.2006.07.025